Implementation and calibration of the TARGET data acquisition system for FAMOUS

von

Nina Laura Höflich

Bachelorarbeit in Physik

vorgelegt der
Fakultät für Mathematik, Informatik und Naturwissenschaften
der RWTH Aachen

im September 2016

angefertigt im
III. Physikalischen Institut A

bei
Univ.-Prof. Dr. Thomas Hebbeker

Erstgutachter:
Prof. Dr. Thomas Hebbeker
III. Physikalisches Institut A
RWTH Aachen

Zweitgutachter:
Prof. Dr. Thomas Bretz
III. Physikalisches Institut A
RWTH Aachen

Betreuer:
Johannes Schumacher
III. Physikalisches Institut A
RWTH Aachen

Contents

1. Introduction

The Pierre Auger Observatory in Argentina is the world's largest observatory for the detection and analysis of extensive air showers, caused by ultra high energetic primary cosmic rays. For that, a hybrid detector is used, composed by 1660 surface detector tanks and 27 air fluorescence telescopes. These telescopes use photomultiplier tubes (PMTs) for their cameras.

A promising alternative to PMTs are silicon photomultipliers (SiPMs). Unlike PMTs, they are robust against the exposure to bright light and their operating voltage is about one order of magnitude lower.
The FAMOUS telescope (*F*irst *A*uger *M*ulti-pixel photon counter camera for the *O*bservation of *U*ltra-high-energy cosmic air *S*howers.) is a prototype for an air fluorescence telescope based on SiPMs. Its camera consists of 61 pixels, each composed by a Winston cone and a SiPM.

To read out all of the pixels simultaneously, the data acquisition system TARGET *(T*eV *Ar*ray with *G*Sa / s sampling and *E*xperimental *T*rigger), originally developed for the Cherenkov Telescope Array (CTA), shall be used in the future.

Within this bachelor thesis, the TARGET module is implemented to FAMOUS. For that, 16 out of the 61 pixels are used. A calibration method for the baseline of TARGET is presented. The calibration is absolutely necessary due to the relatively high baseline fluctuations. In a nightly measurement, the TARGETs performance in combination with FAMOUS is tested by the measurement of Cherenkov light caused by extensive air showers.

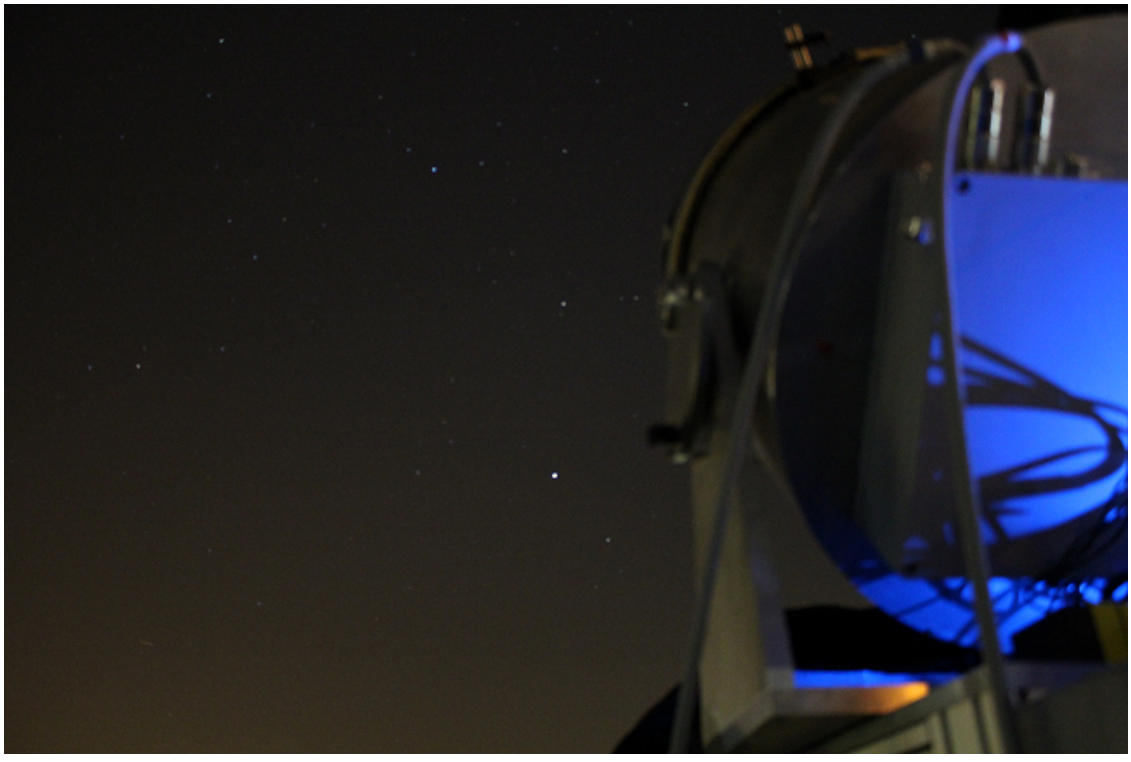

Figure 1.1.: The FAMOUS telescope at night.

2. Cosmic rays

The existence of cosmic rays was discovered by Victor Hess in 1912. In his well known ballon flight experiment, he ascended with a ballon in heights up to 5000 meters and measured the intensity of ionizing radiation by using several electrometers. He discovered that the intensity increases with increasing height. The only explanation for this effect was that the radiation came from outer space [1].

In the following years, his discovery motivated many other experiments.
In 1938, Pierre Auger could demonstrate the existence of extensive air showers. He used two detectors in a distance of several hundred meters and was able to measure particles in both detectors in coincidence. He explained this result with showers of secondary particles, caused by high energetic primary cosmic rays [1].
Today we know that the primary cosmic rays at the top of the atmosphere are composed of stable particles and nuclei. A fraction of almost 90% are protons. The rest are mostly alpha particles, but also heavier elements. Also gamma rays reach the earth and can interact with the atmosphere [2].

2.1. The energy spectrum of cosmic rays

The energy of cosmic rays lies on a scale from MeV up to 10^{20} eV. Though, the flux of cosmic rays depends strongly on the energy of the particle, as can be seen in figure 2.1. Whereas at GeV energies, the flux is about 1000 particles per second and square meter, it decreases rapidly to higher energies, so that at energies of 10^{20} eV, the flux is less than one particle per year and km^2[3].

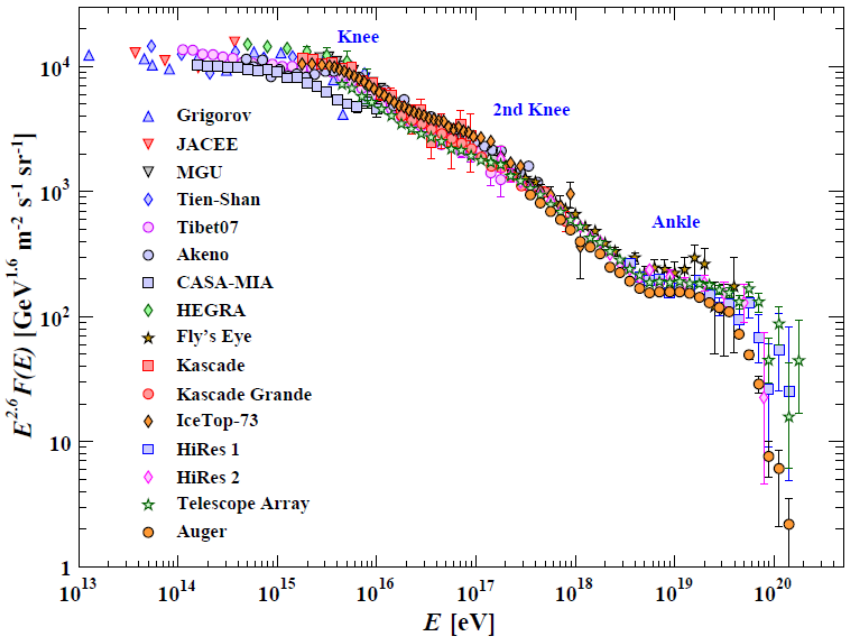

Figure 2.1.: The energy spectrum of cosmic rays at energies higher than 10^{13} eV. The flux is mutliplied by $E^{2.6}$. Taken from [4].

For a wide energy range, the spectrum can be described by a law $dN/dE \propto E^{\gamma}$. For energies below several PeV , the exponent is about $\gamma = -2.7$. At energies between several PeV and about $4 \cdot 10^{17}$ eV , the socalled *knee*, γ decreases to -3.1. Another steepening, the *second knee*, is observed at energies below $4 \cdot 10^{18}$ eV. At higher energies, the *ankle*, the spectrum flattens again ($\gamma = -2.6$) before the flux decreases rapidly to zero at energies of approximately 10^{20} eV [3].

The explanation of these structures is an important part of the modern research. It is assumed that the changes in the spectrum are caused by changes in the acceleration process. For example, the energy of the knee is assumed to be the upper limit for acceleration of particles by galactic supernovae [3].

The fast decrease of the flux at the end of the spectrum could eventually be caused by the GZK-cutoff. The interaction of the cosmic rays with the photons of the cosmic microwave background leads to a cutoff at $6 \cdot 10^{19}$ eV.Above this energy, protons react with the microwave photons and form mainly a Δ^{+}-Resonance [3].

More detailed information about the energy spectrum can for example be found in [5].

2.2. Extensive air showers

When the primary cosmic rays enter the earth atmosphere, they interact with the atmospheric elements like nitrogen or oxygen. Due to this interaction, various secondary particles are produced.

These secondary particles can interact again or decay, so that an air shower is developed.

If the primary particle is a hadron, the reaction with an atmospheric nucleus produces secondary hadrons and initiates a hadronic cascade that contains mostly pions. Via the reaction $\pi^0 \rightarrow \gamma\gamma$ and pair production, an electromagnetic component is developed. Decaying charged pions generate muons and neutrinos, so that a hadronic shower has a significant muon component.

If the primary particle is an electromagnetic particle such as a photon, the dominating interactions are pair production and bremsstrahlung. Because of this, the resulting shower doesn't have a significant muon component [6]. A scetch of the shower structure can be seen in figure 2.2.

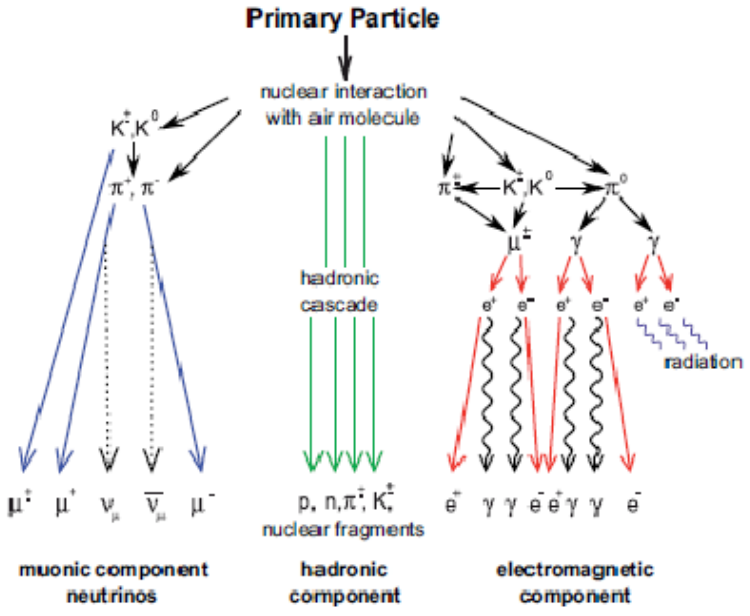

Figure 2.2.: The components of an extensive air shower. Taken from [7].

Shower profile

Whereas an extensive air shower can be expanded over several kilometers in transversal direction, his diameter in longitudinal direction is only in the order of meters [8].
The longitudinal profile, the particle density as a function of the atmospherical slant depth X , of a hadronic shower can be described with the Gaisser-Hillas- function:

$$F(x) = F_{\max}\left(\frac{X - X_0}{X_{\max} - X_0}\right)^{\frac{X_{\max}-X_0}{\lambda}} \cdot e^{\frac{X_{\max}-X}{\lambda}} \tag{2.1}$$

$X - X_{\max}$ describes the distance from the shower maximum, where the maximum shower amplitude $F_{\max}$ is reached. λ describes a typical interaction length and X_0 is a reference depth that is often interpreted as the depth of the first interaction [6].

2.3. Cherenkov light

If a charged particle in a dielectric medium moves faster than the speed of light in the medium, a cone of light is emitted, analogous to the Mach cone for sound waves. The reason for this emission is an asymmetric polarisation of the medium in front of and behind the particle. The aperture angle of the cone can be calculated to:

$$cos(\theta) = \frac{1}{\beta \cdot n} \tag{2.2}$$

with $\beta = u/c$ and the refraction index n. Figure 2.3 illustrates the effect.
The intensity of the Cherenkov radiation (the number of photons per unit of wave length and per unit length of particle path) has the following proportionality:

$$\frac{d^2N}{d\lambda dx} \propto \frac{1}{\lambda^2} \tag{2.3}$$

Because of this, small wavelengths (UV, blue light) dominate in the spectrum [9].

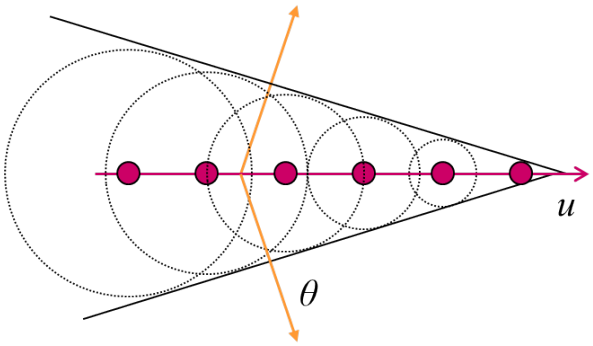

Figure 2.3.: The Cherenkov light cone. u is the particle's velocity. θ is the aperture angle. Taken from [10].

The Cherenkov effect can be used to detect extensive air showers. Since the particles are highly relativistic, they even produce Cherenkov light in the atmosphere. That gives two possibilities to detect them.
First, one can use a tank filled with a light transparent substance with $n > 1$, for example water. If the particle enters the tank, Cherenkov light is emitted and can be detected.
The second method is to detect the Cherenkov light the particle produces in the air. This method was used in this bachelor thesis. As the shower is very flat in longitudinal direction, the particles arrive nearly at the same time on the ground. That means that the Cherenkov light of the shower is a light flash which is only a few nanoseconds long. Because small wavelengths dominate the Cherenkov spectrum, detectors sensitive for UV and blue light should be used.

2.4. Fluorescence light

The charged particles of the air shower can exite the molecules of the atmosphere, mostly nitrogen. During the relaxation process of the molecules, fluorescence light with characteristic wavelengths is emitted isotropically. The spectrum of nitrogen can be found in figure 2.4. The wavelengths of the emitted light lie in the range of 300 to 430 nm. The number of emitted fluorescence photons is proportional to the electromagnetic energy losses of the charged particles:

$$\frac{d^2N_\gamma}{dX\,d\lambda} = Y(\lambda, T, p, u) \cdot \frac{dE}{dX} \tag{2.4}$$

With the energy deposit $\frac{dE}{dX}$ and the fluorescence light yield Y, assumed to be independent of the electron energy E [11]. The fluorescence yield at a given wavelength describes the number of photons at this wavelength emitted per unit of energy loss by charged particles and is a function of the atmospheric parameters: temperature T , pressure p and humidity u. [12]
The detection of fluorescence photons is an important part of the air shower analysis. The functionality of fluorescence detectors is explained in the next section at the example of the Pierre Auger Observatory.

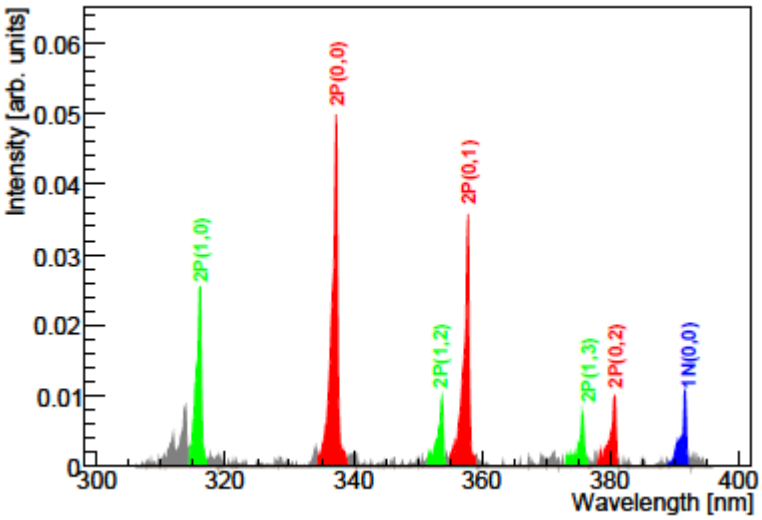

Figure 2.4.: The fluorescence spectrum of nitrogen between 300 nm and 400 nm in dry air at 1013 hPa. Adapted from [13]

2.5. The Pierre Auger Observatory

The Pierre Auger Observatory near Malargüe, Argentina consists of 1660 water cherenkov tanks and 27 air fluorescence telescopes, allocated on an area of 3000 km^2. The combination of the surface detector tanks and the fluorescence telescopes allows to detect and analyze air showers with best accuracy [12].
In figure 2.5, the arrangement of the detectors can be seen.

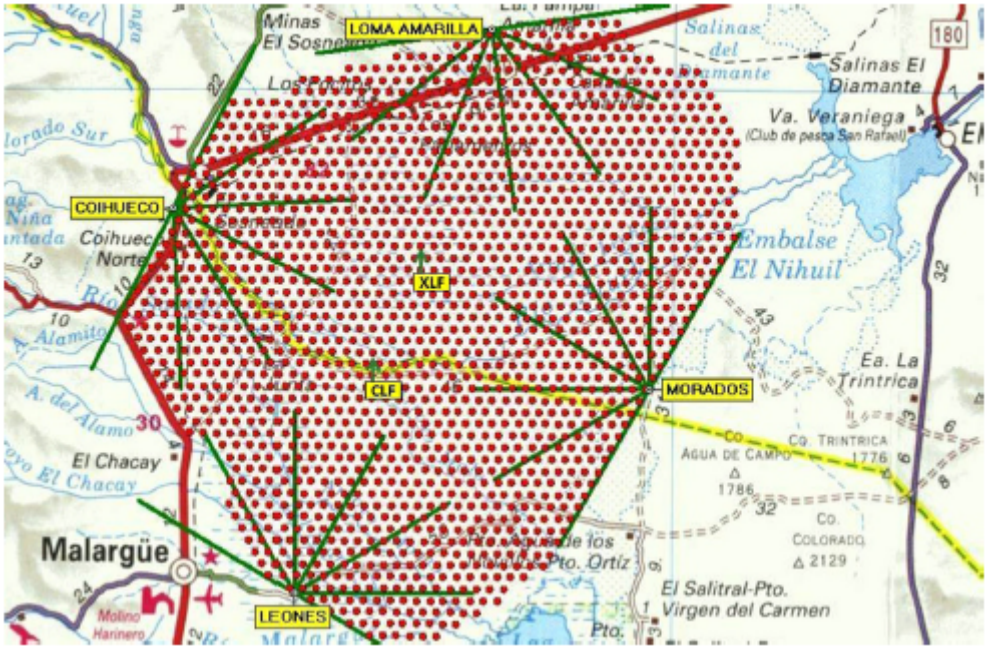

Figure 2.5.: The arrangement of surface and fluorescence detectors. The red points represent the surface detectors. The orientation of the flouorescence telescopes is depicted by the green lines. Adapted from [14].

The water Cherenkov detectors use the Cherenkov effect to detect shower particles, as described in section 2.3. Each of the tanks contains 12,000 l of pure water and has a reflective inner surface. The produced Cherenkov light is collected by three photomultiplier tubes (PMTs) with a diameter of nine inch each. The PMTs look downwards into the water in the tank and are symmetrically distributed at a distance of 1.2 m from the center of the tank. The duty cycle is nearly 100 % [15].
The technique used to detect ultra high energy cosmic rays ($E > 10^{18}\,\mathrm{eV}$) using fluorescence light of nitrogen is also used in other projects like the Fly's Eye experiment.
To reconstruct the longitudinal development profile $\frac{dE}{dX}$ of the air shower, the rate of fluorescence emission in dependence of the atmospheric slant depth X is measured (see formula (2.4)) . By integrating over the profile, the electromagnetic energy dissipation can be calculated, which is about 90 % of the total primary cosmic ray's energy.
To measure the axis of an air shower with fluorescence detectors, it is best to use more than one telescope. Then, the shower axis can be calculated from the intersection of the shower planes measured by the individual telescopes. If only one telescope is used, one can calculate the shower axis by using the timing imformation t_i of each triggered camera pixel of the telescope:

$$t_\mathrm{i} = t_0 + \frac{R_\mathrm{p}}{c} \cdot tan[(\chi_0 - \chi_\mathrm{i})/2] \tag{2.5}$$

As illustrated in figure 2.6 , t_0 is the time of the smallest distance R_p between shower front and camera. χ_0 describes the angle between the horizontal plane and the track and χ_i is the angle between the horizontal plane and the pointing direction of each pixel.
After the shower axis is reconstructed, the light collected by the telescopes' cameras as a function of time can be used to calculate the energy deposit as a function of the slant depth [12].

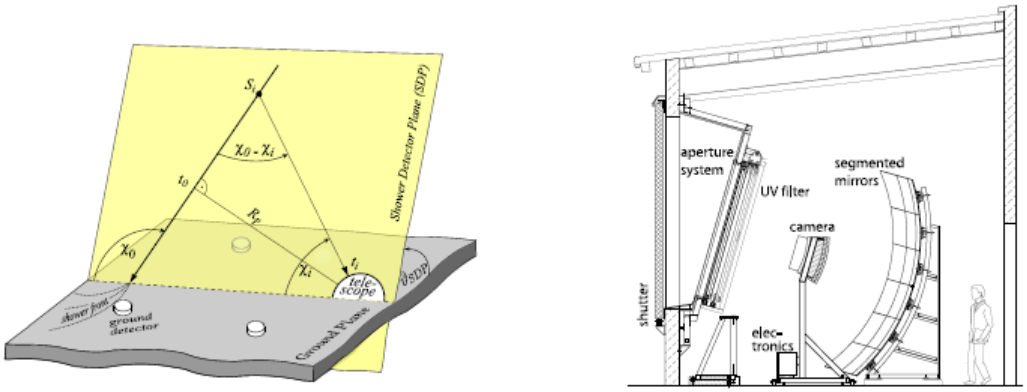

Figure 2.6.: Left: Geometrical reconstruction of the shower axis. **Right**: Schematic picture of a fluorescence telescope of the Pierre Auger Observatory. Both taken from [12]

The fluorescence detector of Auger contains four observation sites, three with six and one with nine independent fluorescence telescopes. Every telescope has a field of view of 30° x 30° in azimuth and elevation. The telescopes are combined in a way that the total field of view of the six telescopes is 180° in azimuthal direction. In figure 2.6, the setup of a telescope is shown. The fluorescence light enters the telescope through a large UV-passing filter. By a segmented mirror, the light is focused on the camera, which contains 440 pixels with photomultipiers as light sensors [12].
Further information on the Auger observatory and the shower detection techniques can be found in [12, 15].

3. The FAMOUS Telescope

Today, the most often used light detectors in particle physics are photomultiplier tubes (PMTs). They are extremly sensitive light detectors, which allow to detect single photons. Unfortunately, they need a high voltage of a few kV to operate. Aditionally, photomultiplier tubes can be permanently damaged if they are exposed to bright light.

An alternative are silicon photomultipliers (SiPMs). These detectors reach the same perfomance as PMTs, but only need a voltage of several tens of volts to operate. Besides, silicon photomultipliers are robust against the exposure to bright light. This allows to measure also at nights with bright moon light, which is more difficult if PMTs are used [16].
The FAMOUS (*F*irst *A*uger *M*ulti-pixel photon counter camera for the *O*bservation of *U*ltra-high-energy cosmic air *S*howers) telescope, constructed at III. Phys. Institut A at RWTH Aachen University, is a prototype of a SiPM based fluorescence telescope. The camera contains 61 pixels that allow the detection of both Cherenkov and fluorescence light of extensive air showers.

In this chapter, the properties of silicon photomultipliers and the FAMOUS telescope are described. Additionally, the functioning of the data acquisition system TARGET7, which is currently used in FAMOUS, is explained.

3.1. Silicon photomultipliers

3.1.1. The basic functionality

Like many other semiconductor devices, SiPMs are based on p-n junctions.
In a p-n junction, a n-doted and a p-doted semiconductor are brought together. Because of the higher concentration of electrons in the n-region and of holes in the p-region, the electrons diffuse to the p- region and the holes to the n-region, leaving the ionized donors and acceptors behind. This leads to an electric field across the junction. The electric field creates a reverse drift current of the electrons and holes, which cancels out with the diffusion in thermal equilibrium. Also, the electric field leads to a layer without free charge carriers in the middle of the p-n junction (the socalled depletion layer)[17], as can be seen in figure 3.1.

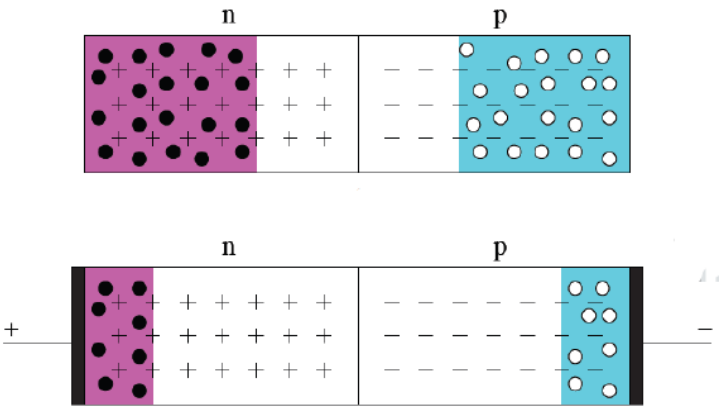

Figure 3.1.: Top: The p-n junction without a reverse bias voltage. Below: The p-n junction with a reverse bias voltage, which leads to a larger depletion layer (white). Taken from [18]. Edited by the author.

The depletion layer allows the detection of photons and charged particles. If a sufficiently energetic particle crosses the layer, it can create an electron-hole-pair (eh-pair) that is separated because of the electric field. This leads to a (very small) photo current if the sides of the junction are connected via an amperemeter.

Unfortunately, the current created by single photons is much to small to be measured. That makes an amplification necessary. This can be done by the application of a reverse *bias voltage* V_b across the section, so that the strength of the electric field and the width of the depletion layer increases.
If the bias voltage is high enough, the electron of the eh pair created by an entering photon gain enough energy in the field to produce secondary eh holes pairs. These new charge carriers can do the same, so that an avalanche is developed. The holes will not contribute to the avalanche, since they are less mobile and not enough accelerated. The resulting amplification is about 50-200.

If single photons should be detected, a higher amplification is necessary. This is possible by increasing V_b above the socalled *breakdown voltage* V_bd. Then, the diode operates in the *Geiger mode* and is therefore called *G*eiger-mode *A*valanche *P*hoto *D*iode (G-APD). Now, electrons *and* holes gain enough energy to produce secondary eh-pairs. This leads to a diverging avalanche, that need to be stopped externally. This can be done by connecting the diode in series with a quenching resistor. The increasing current leads to an increasing voltage drop at the resistor, so that the voltage over the diode falls below the breakdown voltage and the avalanche ends. During this recovery time, new incoming photons will produce no or smaller avalanches.
In Geiger mode, the produced charge Q in the avalanche and so the measured signal is independent of the number of primary eh pairs and given by:

$$Q = C_\mathrm{GAPD} \cdot V_\mathrm{ov} = C_\mathrm{GAPD} \cdot (V_\mathrm{b} - V_\mathrm{bd})\,, \tag{3.1}$$

with the *overvoltage* V_ov and the capacitance of the G-APD C_GAPD. The reached amplification lies between 10^5 and 10^7 [17]. The values for the breakdown voltage vary from manufacturer to manufacturer [19]. For the SiPMs used in the FAMOUS telescope, V_bd is approximately 65 V at room temperature, see also section 3.2.

If the proportionality of the output signal to the input signal shall be restored, it is necessary to use more than one G-APD. In an SiPM, many G-APDs with their individual quenching resistors are connected in parallel. If several photons reach the SiPM simultaneously, the photons can be detected by different cells (G-APDs). Every cell will produce a characteristic charge Q. The output signal of the SiPM is then the sum of charges [17]. That allows to reconstruct the number of incoming photons. Nevertheless, several effects have to be considered.
One of those effects is the saturation. As the SiPM consists of a finite number of G-APDs, there is an upper limit for the maximum rate of detected photons, namely when all cells are firing. More effects are discussed in the next sections.
In figure 3.2, a photography and a schematic scetch of an SiPM are shown. Additionally, an oscilloscope screenshot of many overlapping, amplified SiPM signals is presented in figure 3.3. It can be seen that there are different signal heights with stable distances. The smallest height corresponds to one triggered SiPM cell (one cell breakdown), the second one corresponds to two and so on. The number of triggered cells is often given in photon equivalents (p.e.), as one photon can trigger one SiPM cell[1].

[1] If correlated noise is ignored, see section 3.1.4.

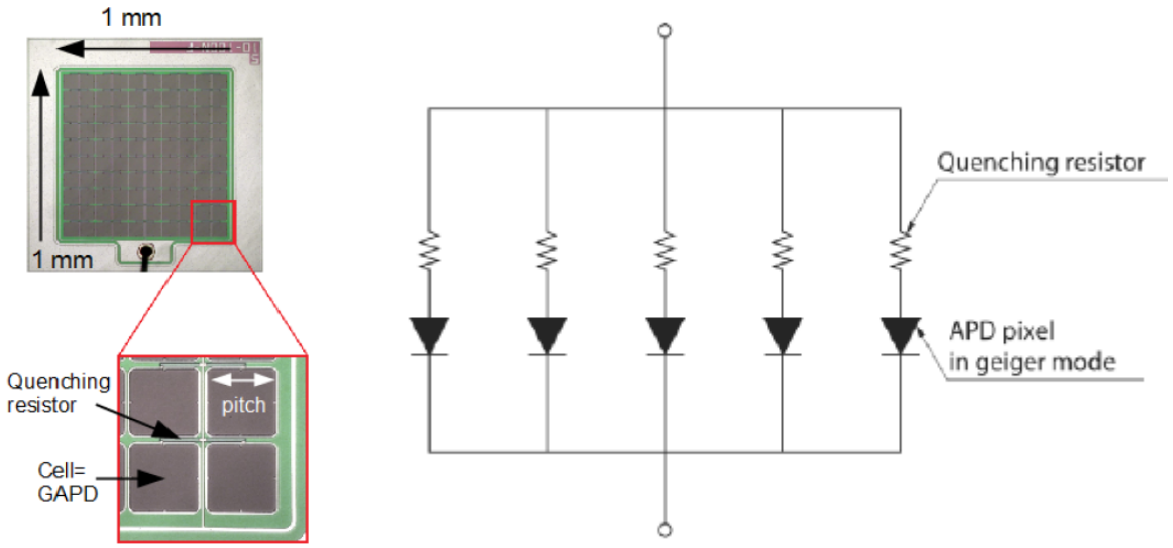

Figure 3.2.: Left: Photography of a SiPM with 100 cells with zoom into 4 cells. Taken from [17]. **Right**: Schematic layout of a SiPM. Taken from [8].

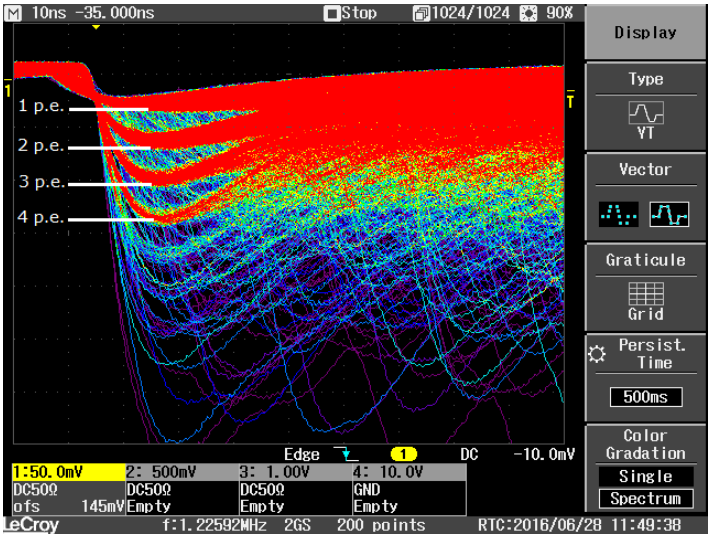

Figure 3.3.: Oscilloscope screenshot of overlapping, amplified SiPM signals recorded by the author. Voltage (div $= 50\,\mathrm{mV}$) is plotted against time (div $= 10\,\mathrm{ms}$). The event rate is color coded. The 1 p.e. to 4 p.e. signals can be seen clearly. The picture was made with a LECROY WJ 354A oscilloscope with $50\,\Omega$ load.

3.1.2. Temperature dependence of the breakdown voltage

The breakdown voltage, the minimum bias voltage necessary for the Geiger Mode, depends on the temperature. The connectedness is found to be linear in a wide temperature range and given by

$$V_{\mathrm{bd}}(T) = V_{\mathrm{bd}}(T_0) + \beta(T - T_0) \tag{3.2}$$

with a reference temperature T_0. The constants β and $V_{\mathrm{bd}}(T_0)$ depend on the device's properties, but almost not on other physical quantities [19, 20].
The temperature dependence of V_{bd} makes it necessary to adjust the bias voltage with temperature at the SiPMs. Otherwise, the gain, the produced charge per GAPD, of the SiPM will change during the measurement, just as the photon detection efficiency (see section 3.1.3).

3.1.3. Photon detection efficiency

The photon detection efficiency (PDE) describes the probability that an incoming photon leads to an output signal of the SiPM. The PDE is a function of the overvoltage V_{ov} and the wavelength λ and can be expressed by:

$$PDE(V_{\text{ov}}, \lambda) = f_{\text{Geom.}} \cdot QE(\lambda) \cdot P_{\text{Geiger}}(V_{\text{ov}}) \tag{3.3}$$

f_{Geom} is the geometrical fill factor. Parts of the SiPM's cells are not sensitive to light, i.e. because of the quenching resistors of each cell. The geometrical fill factor describes the fraction of the light sensitive area of the SiPM and can reach up to 80%, depending on the SiPM's layout.

QE is the quantum detection efficiency. This parameter describes the probability that an incoming photon creates an eh pair in the depletion region. As absorption is the reason for the creation, the quantum detection efficiency depends on the wavelength of the photon. [21].

The probability that the created charge carriers trigger an avalanche is considered by P_{Geiger} and depends on the overvoltage, as explained in the last section. If the overvoltage is large enough, the probability is nearly 100% [22].
At the moment, acquirable SiPMs reach PDEs of approx. 50 % [2].

3.1.4. Noise phenomena

SiPM show different noise phenomena. It is distinguished between random thermal noise and correlated noise, where one breaking cell causes further cell breakdowns. This can happen either instantaneously (*optical crosstalk*) or delayed (*afterpulsing*). Also a combination of afterpulsing and optical crosstalk is possible (*delayed crosstalk*).

Thermal noise

Not only photons, but also thermal exitation can generate eh pairs in SiPM cells. This leads to a relatively high dark count rate in the range of kHz up to MHz at room temperature, depending on the SiPM type and size. The FAMOUS' SiPMs, each an array of four $3 \times 3\,\text{mm}^2$ SiPMs, have a dark rate of approximately 1 MHz at room temperature.
As the probability for thermal exitation increases with rising temperature, the dark rate will increase, too.

Optical crosstalk

If an avalanche is triggered in one SiPM cell, the recombination of eh- pairs can produce photons. These photons can cause adjacent cells to break down.
The crosstalk probability was studied in [17] and is a function of the overvoltage. It also depends on the SiPM size and the cell pitch, respectively the size of the active area of the SiPM. The larger the active area is, the higher is the probability that a photon produced during a cell breakdown causes another cell to break down. That means that the crosstalk probability increases with the increase of the active area [17]. The functional dependence can be seen in figure 3.4.

[2] e.g. SensL J-Series. [23]

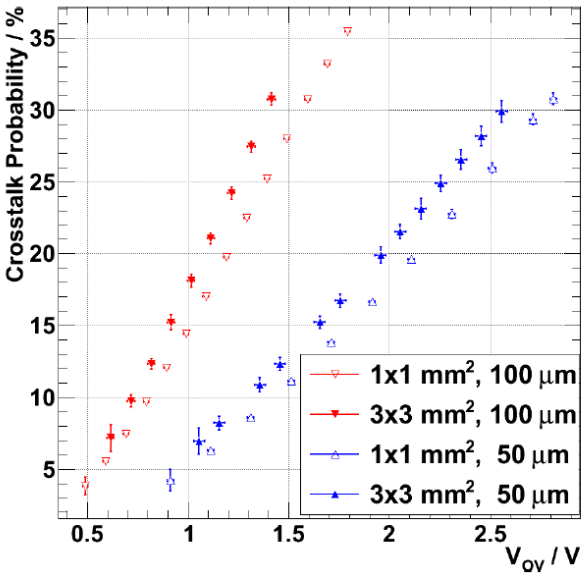

Figure 3.4.: The crosstalk probability as a function of the overvoltage. The SiPMs had a size of $1 \times 1\,\mathrm{mm}^2$ or $3 \times 3\,\mathrm{mm}^2$ and a cell pitch of $50\,\mu$m or $100\,\mu$m. An increase of the overvoltage leads to an increase of the probability. For large SiPMs with high cell pitches (large active area), the crosstalk probability is higher, as explained in the text. Taken from [17].

The optical crosstalk can be used to calculate the gain, that means the produced charge per avalanche, of a SiPM. Also the crosstalk probability can be determined. For that, measurements in darkness are performed. Thermal noise lead to a breakdown in one SiPM cell. Optical crosstalk can now cause further cell breakdowns instantaneously. The output signal of the SiPM is the sum of charges of the fired cells and an integer multiple of the charge produced of one cell [3]. If many measurements are done, a histogram of signal heights (*finger spectrum)* can be created. An idealized example is shown in figure 3.5. Several peaks (*fingers*) can be seen. The highest peak on the left side (smallest charge) is the charge produced by one triggered SiPM cell (1 p.e. peak, see section 3.1.1). The other peaks are caused by optical crosstalk. The peak distance is the gain. The relative height of the other peaks compared to the one- cell-peak is an estimation for the crosstalk probability. A more detailed discussion can be found in section 4.3.

[3] Here it is assumed for simplification that every cell produces the same amount of charge.

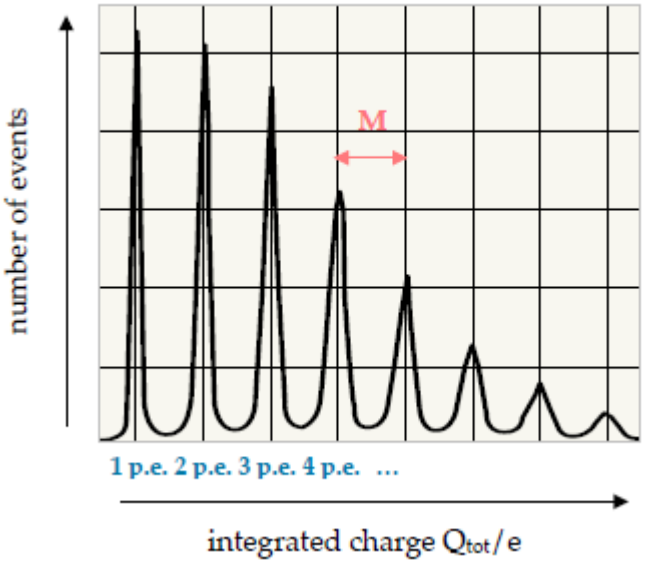

Figure 3.5.: Idealized finger spectrum. The absolute frequency of the produced charge in several thousand events is plotted. The highest peak on the left is the charge of one cell breakdown (1 p.e. peak). The other peaks are caused by optical crosstalk. Taken from [24].

Afterpulsing

During an avalanche in a SiPM cell, individual charge carriers can be trapped in extra energy levels in the forbidden zone between valence and conduction band. These levels are caused by impurities and defects in the silicon crystal. After a statistical time delay, the charge carrier is released. If this release happens after the avalanche is waned, a new avalanche can be triggered. This effect was studied in much more detail in [17].
The afterpulsing probability increases with the overvoltage and depends on the SiPM size and cell size [17].

Both afterpulsing and optical crosstalk can lead to an overestimation of the measured signal rate and have to be considered in precise measurements.

3.2. The baseline design of FAMOUS

The main components of the FAMOUS telescope are a Fresnel lens as refracting optics and a 61 pixel-camera in the focal plane with SiPMs as light detectors and Winston cones to collect more photons. The pixels are arranged in a hexagonal structure.
The Fresnel lens has a diameter and also a focal length of 510 mm. The Fresnel lens is used because it is much thinner than a spherical lens of the same diameter and focal length. This leads to less absorption and weight.
Each pixel of the camera consists of an aluminium Winston cone (hollow, round-to-round, entrance radius $r_1 = 6.7\,\text{mm}$, exit radius $r_2 = 3\,\text{mm}$) and a Hamamatsu S12573-100X array of four $3 \times 3\,\text{mm}^2$ SiPMs. Therefore, the effective active area is $6 \times 6\,\text{mm}^2$. The cell pitch is $100\,\mu\text{m}$. Every pixel has a field of view of $1.5\,^\circ \times 1.5\,^\circ$ [25].
Additionally, three blind pixels are placed in the telescope. That allows to check the SiPM noise during the measurement. For the blind pixels, the same SiPM arrays are used.
All 64 SiPMs are placed on a board that contains i.a. capacitors for each SiPM. These capacitors filter DC components of the signals out, leading to an AC-coupled read-out. The SiPM board is connected to an adapter board. This allows the read-out of the SiPMs via individual SMA-cables, which can be affixed to the board. For 20 SiPMs, this was done in this bachelor thesis (see section 4.1.1). As 64 individual cables are impractical , a new adapter board was designed by A. Bogner during his bachelor thesis [26]. It allows to read out the 64 SiPMs via four flat ribbon cables with 16 channels each and can be used in future measurements.
As readout electronics, the TARGET electronic was implememented during this thesis. More information on the TARGET are given in the next section and in chapter 5.
The voltage supply of the SiPMs is controlled by a power supply unit developed at III. Physikalisches Institut A, RWTH Aachen University. A built-in microcontroller and 64 analogue temperature sensors allow voltage correction for temperature changes. This guarantees a constant, adjustable overvoltage and therefore a constant, adjustable gain during a measurement. [19, 25]
The typical overvoltage for the Hamamatsu SiPMs used is 1.4 V. The communication with the power supply is done via Ethernet.
In figure 3.6, a photography of the telescope and a schematic camera layout are shown.

Figure 3.6.: Left: Photography of FAMOUS. **Right**: Schematic camera layout. The 61 circles symbolize the 61 pixels. They are arranged in a hexagonal structure. For better orientation, the pixels are numbered. The three pixels outside the hexagon symbolize the three blind pixels.

3.3. The data acquisition system TARGET

TARGET (*T*eV *Ar*ray with *G*Sa / s sampling and *E*xperimental *T*rigger) is a data acquisition system developed for the readout of photon sensors at the CTA (*C*herenkov *T*elescope *A*rray)-Observatory. With its sampling rate in the order of 1 GSa/s, the 64 input channels and an internal trigger, the TARGET module can be used for the readout of the 64 FAMOUS SiPMs. The latest version of TARGET is called TARGET7. At the moment, only a prototype of TARGET7 is available and was used in this thesis.
In this section, the setup and basic properties of the TARGET board are presented in a short way. More information can be found in section 5.2 and in [27].

3.3.1. Setup and properties

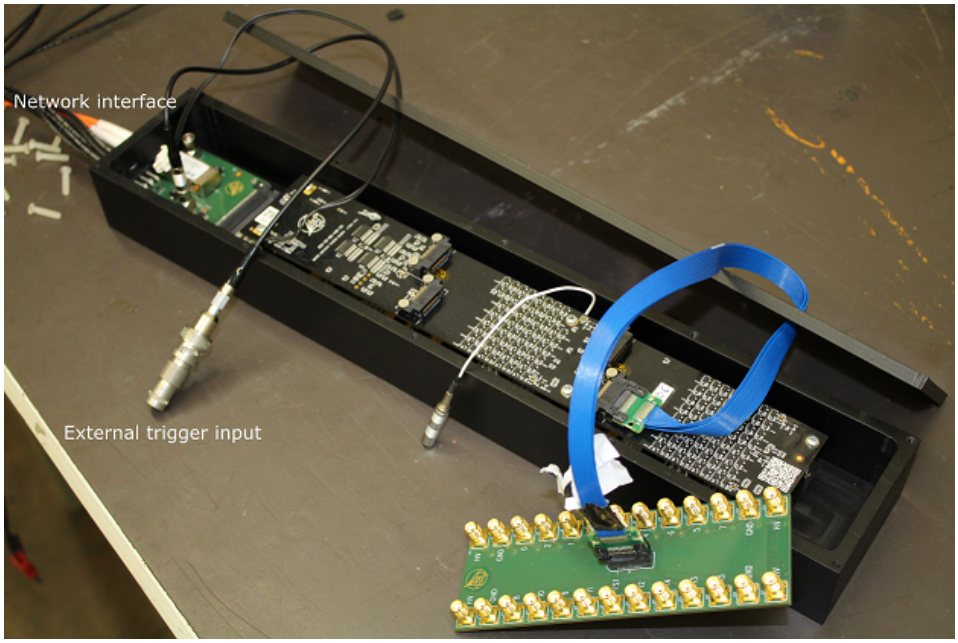

Figure 3.7.: Photography of the TARGET7 module. With the green adapter board and the blue flat ribbon cable, 16 SMA cables can be connected to the TARGET board. At the moment, it is not possible to connect more than 16 cables to the board, as there is only one adapter board available. The TARGET itself is composed of two boards on top of each other, where all components are affixed. The black housing was made by the workshop of III. Physikalisches Institut B, RWTH Aachen University.

The TARGET7 module contains four TARGET7-ASICs (*A*pplication- *S*pecific *I*ntegrated *C*ircuit). Every ASIC reads out the signal of 16 channels (i.e. 16 FAMOUS SiPMs) simultaneously. The signal is sampled with a typical rate of 1 GSa/s, but also other rates can be implemented. The samples are stored in an analogue ring buffer that has 16,384 memory cells for each channel. The digitalisation via an ADC (*A*nalogue *D*igital *C*onverter) is done when the samples are read out. The ASICs and the readout are controlled by an FPGA (*F*ield *P*rogrammable *G*ate *A*rray) [28].
Because of the high number of memory cells, it is theroretically possible to measure about 16 μs long traces if the sampling rate is 1 GSa/s. As the TARGET used here is only a prototype, only 448 samples can be read out for each channel, accordingly only 448 ns at 1 GSa/s.
Each input channel of the ASIC boards has a signal line and a reference line. The reference line allows to add a DC-offset (*Vped* = *voltage pedestal*) on the signal on every channel. This is useful if negative input signals have to be measured. The ADC can only work with positive signals. The Vped can shift a negative signal in the positive range, so that the ADC can digitize it [27, 28].

To amplify the input signal before the digitalisation, the TARGET module contains internal preamplifiers. They also shape the signal, as it is shown in [27].
The sample readout only starts if a trigger signal is given. For that, the TARGET module has different trigger modes, as it is described in the next section.
The communication and data transfer is done via Ethernet. For that, the TARGET has a network interface.
Via an adapter board and a flat ribbon cable, SMA cables can be connected to the TARGET. Unfortunately, only one adapter board is available at the moment. This limits the connectable SMA cables to 16.

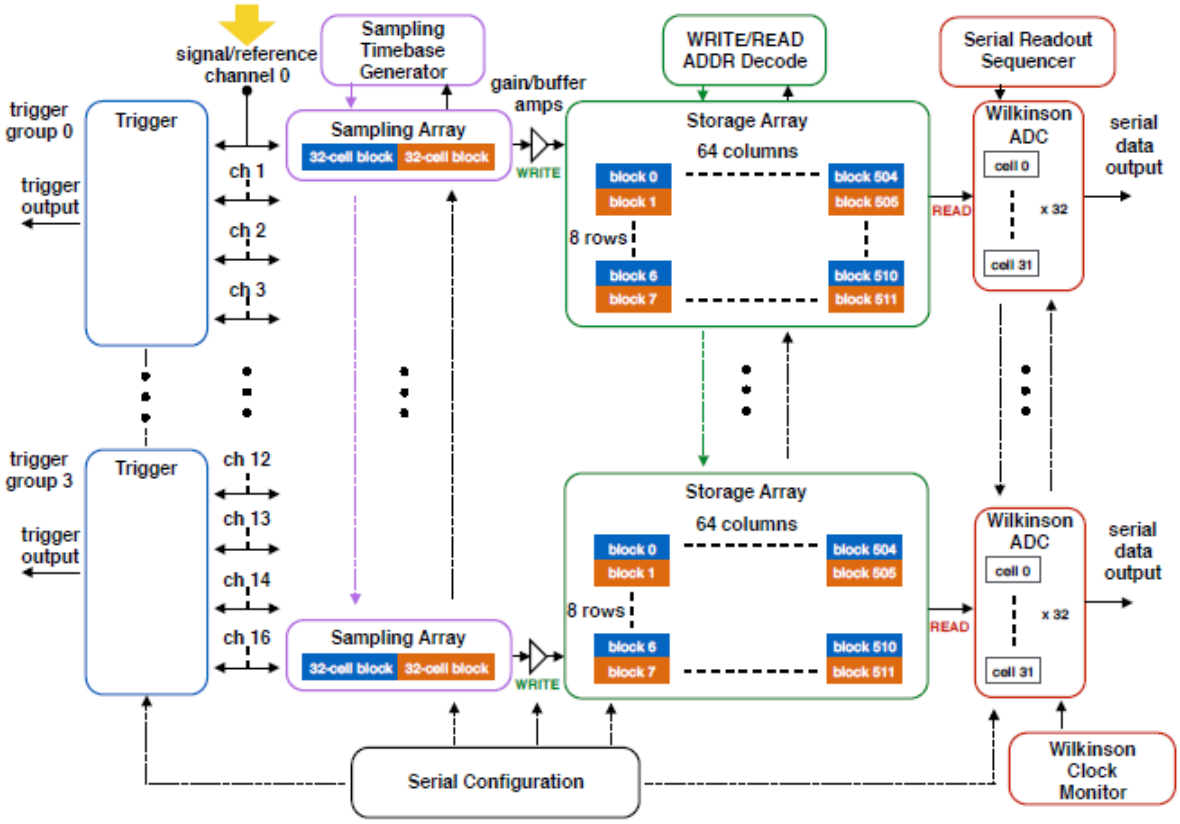

Figure 3.8.: Functional block diagram of the TARGET7 ASIC. The samples are first temporary buffered in one of the two blocks of the sampling array. Both blocks contain 32 memory cells. If the block is full, the samples are transferred into one of the 512 blocks (with 32 cells each) of the storage array. During this process, the second block of the sampling array is filled. This warrants a continous sampling. As the blocks of the storage array are filled sequentially, a ring buffer is formed. The samples in the memory blocks are read out on demand and digitized by an ADC [27, 28]. Taken from [28].

3.3.2. Trigger modes

For data acquisition, three different trigger modes of the TARGET7 module can be used.

First, there is the socalled *hardsync trigger*. If this trigger type is used, an internal clock will trigger the data acquisition with a frequency of approximately 120 Hz. The readout of the ring buffer always starts at the same memory cell (henceforth called *First Cell*), in contrast to the other trigger types.

The second possible trigger mode is the *external trigger*. If this mode is activated, the TARGET waits for an external pulse at the external trigger input. If a pulse is distinguished, the data acquisition starts.
If the pulse should be detected as trigger signal, the pulse width must be at least 8 ns and the amplitude must be larger than 2 V [27].
As the trigger pulse arrives at different times of the internal cyclus of sampling, the First Cell fluctuates from measurement to measurement. This has to be considered in the baseline calibration, see also section 5.2. For that reason, the First Cell of a measurement is stored.

The TARGET is also able to trigger directly on a measured signal, for example a SiPM pulse. For this *internal self trigger*, always four channels of an ASIC are taken together into one trigger group. The measured signals on these channels are summed up. If the sum is larger than a adjusted trigger threshold, the data readout starts. Additionally to the threshold, a reference voltage can be implemented that is also added to the trigger groups. To minimize the trigger noise, threshold and reference voltage have to be optimized [27].
The commissioning of the internal self trigger is done in [29]. The self trigger is not used in this bachelor thesis.

4. Preparation of the FAMOUS camera

In this section, the preparation of the FAMOUS camera for the measurement of Cherenkov light of extensive air showers is described. All measurements and the analysis were done in cooperation with B. Pestka.
All pixels used were tested on their functionality. Also, dark rate measurements were done with the use of an oscilloscope. As the oscilloscope is a professional, commercial data acquisition system, the results of the data analysis should be the best possible result.

4.1. Setup

To test the functionality and do dark rate measurements, the FAMOUS SiPMs have to be connected to an oscilloscope. In figure 4.1, a photography of the setup can be seen. The SiPMs of FAMOUS are connected to an adapter board, as described in section 3.2. On this board, 20 SMA cables were soldered. These cables can be connected via an amplifier board to the oscilloscope.
The communication with the FAMOUS PSU is done via Ethernet with the laptop.
To shield the SiPMs of FAMOUS from light, which is very important for dark rate measurements, the telescope has a light tight, removable capping. Furthermore, the telescope is placed in a room well darkened by venetians and the light is turned off. As the probability for the noise phenomena depends on the temperature, the room temperature was kept constant by an air-conditioning.
Further information and details on the setup are given in the following subsections.

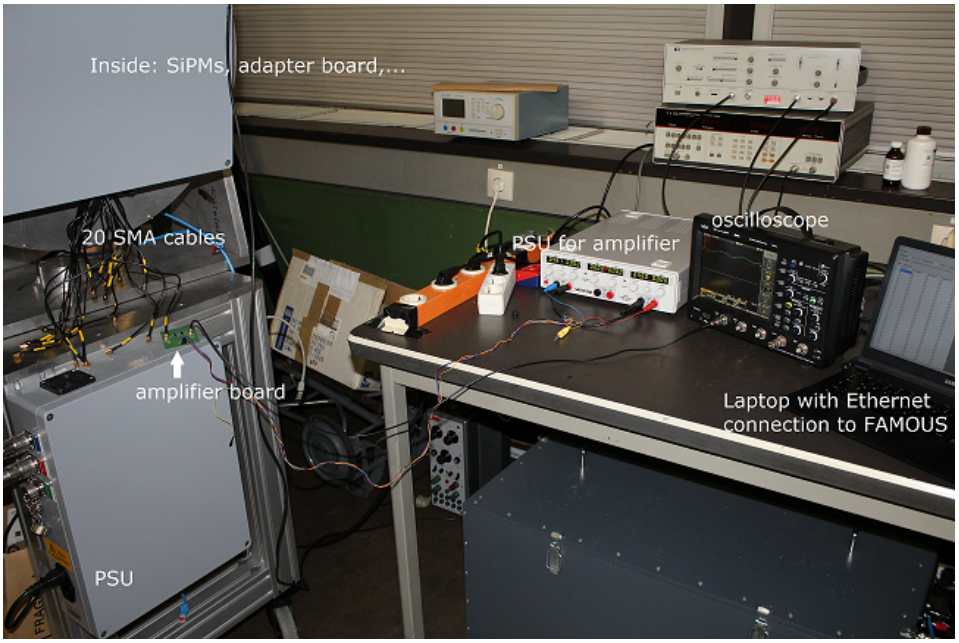

Figure 4.1.: Overview of the setup. The SiPMs are connected to an adapter board (inside the grey box). On the adapter board, 20 SMA cables were applied. One of these cables (i.e. one SiPM) is connected via an amplifier board to the oscilloscope. The amplifier board is connected to a voltage supply. The voltage supply of the SiPMs is controlled with the laptop via Ethernet.

4.1.1. Wiring of the SiPMs

All 64 SiPMs are connected to an adapter board, as described in section 3.2.
20 SMA cables with a length of approx. 50 cm were soldered on the board by B. Pestka and N. Höflich. 16 out of these 20 cables can be connected to the TARGET (see section 3.3.1). The connected cables are chosen in a way that all central pixels of the FAMOUS camera can be used for measurement (see figure 4.3). This choice is useful, as the Fresnel lens has the best imaging properties in the middle. Besides, this choice enables a continuous detector area.
Also a blind pixel is endued with a cable to be able to record the SiPM's dark rate parallel to the measurement.
As four pixels more are equipped with cables as can be connected to the TARGET board, the layout used for a measurement can be changed flexible within certain limits.
In figure 4.2, a photography of the adapter board with soldered SMA cables is shown. Additionally, in figure 4.3 the pixels of the FAMOUS camera equipped with cables are schematically depicted.

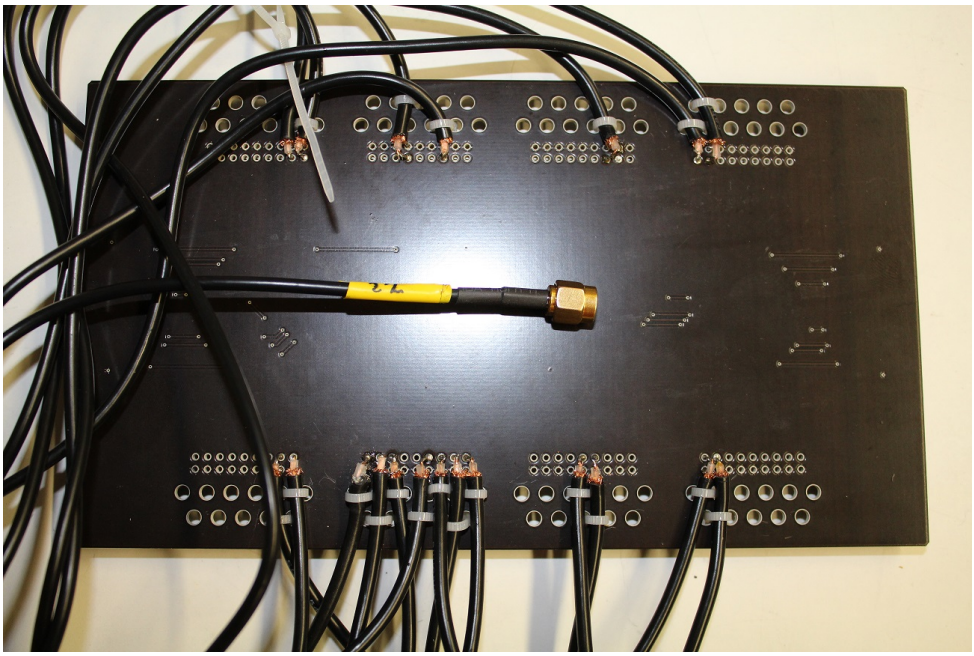

Figure 4.2.: Photography of the adapter board with the connected SMA cables. Every cable was labelled with the pixel number of the FAMOUS camera. Made by N. Höflich and B. Pestka

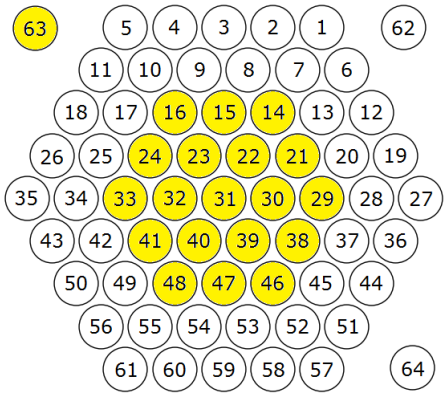

Figure 4.3.: Schematic depiction of the pixels equipped with SMA cables (in yellow). 19 pixels of the camera and one blind pixel were selected.

4.1.2. Amplification and recording of the signals

Each of the SiPMs can be connected via an amplifier board with the oscilloscope. Without amplification, the signals would be too small to be distinguished from the electronic noise.

The amplifier board was constructed by J. Schumacher at III. Physikalisches Institut A, RWTH Aachen [30]. It needs a supply voltage of $5 - 6\,\mathrm{V}$. This voltage is provided by a *Rohde&Schwarz HM7042-5 triple power supply*. The amplification is nearly independent of the supply voltage. Nevertheless, the supply voltage is kept constant during the measurements.

For data recording, a *LECROY WaveJet 354 A* digital oscilloscope with 500 MHz bandwidth and $50\,\Omega$ DC input coupling is used. The amplified SiPM signal is read via one of the four oscilloscope's channels. Each channel has a vertical resolution of 8 bit. Therefore, 2^8 different voltage values can be distinguished within the full scale. The full scale consists of 8 vertical divisions with an adjustable step size. The DC gain accuracy is $\pm 1.5\,\% + 0.5\,\%$ of full scale.
The oscilloscope consists of an internal trigger system. In the measurements, it was triggered on the falling edge of the pulses.

4.2. Test of Functionality

To check the functionality of the SiPMs and the connection of the SMA cables to the adapter board, a laser pointer can be used.

Measurement procedure

The measurement is done in darkness. One pixel is connected to the oscilloscope as described in the last section. The FAMOUS power supply is turned on and an overvoltage of 1.4 V is set. The light-tight capping of the FAMOUS telescope, which protects the lens, is removed.
First, the oscilloscope signal in darkness with removed capping is measured. After that, a laser pointer is aimed through the lens of the telescope to the connected pixel. Again, the oscilloscope signal is measured.
The laser pointer gives the possibility to illuminate exactly one pixel. Of course, the other pixels will also measure light because of reflections, but the majority of light arrives on the targeted pixel. To check this, the laser pointer was directed on a pixel adjacent to the connected one and the signal of the connected pixel was measured again with the oscilloscope. These measurements were done for every pixel equipped with SMA cables.

Measurement results

In figure 4.4 on the left, an example for the signal of one of the pixels recorded with the oscilloscope is presented. Large SiPM pulses can be seen. Similar signals were measured for all pixels. The trigger rate of the oscilloscope is about 3 MHz. As the measurement was done with the capping of FAMOUS removed, photons coming from residual light in the room reach the SiPM and can be detected. This causes the high detection rate in comparison to the dark noise rate of approximately 1 MHz. Because the SiPM signals reach the oscilloscope, there has to be a connection between a pixel and the oscilloscope. Nevertheless, it is not yet proved, that the right pixel is connected, and not another one. This was checked with the laser pointer.
In figure 4.4 in the middle, an exemplary oscilloscope screenshot of the SiPM signal, while the connected pixel is illuminated by the laser pointer, is shown. No SiPM pulses can be seen. This has two reasons. First, the SiPM is hit by so much light that the PSU of FAMOUS automatically reduces the bias voltage below the breakdown voltage to protect SiPM and electronic. Therefore, the SiPM does not operate in Geiger mode so that only very small pulses are produced. The second reason are the capacitors on the SiPM board (see section 3.2). As so many photons reach

the SiPM, the cells are constantly firing. Therefore, the output signal is de facto a DC current that is filtered out by the capacitors.
On the right side in the figure, the SiPM signal that is recorded if not the connected pixel, but a neighbouring pixel is illuminated, is presented. In this case, small pulses can be seen. The trigger rate is only 50 kHz. The cause is that the PSU does not reduce the bias voltage for the whole measurement, as less light reaches the pixel. As still many photons reach the pixel due to reflections and insufficient sighting with the laser pointer, the SiPM often saturates, so that the output signal has a large DC component, which is filtered out by the capacitors on the SiPM board. Therefore, the registered signals and the trigger rate are much smaller than normal, as can be seen in the figure.

The combination of both measurements proves the correct wiring of the SiPMs, as it can be clearly differentiated between a hit of the connected pixel and a miss. For all pixels, the oscilloscope images look similar to the presented ones. If the allegedly connected pixel is targeted, no SiPM pulses can be seen on the oscilloscope. If a neighbouring pixel is targeted, very small pulses can be seen. That means that all pixels are connected in the right way.

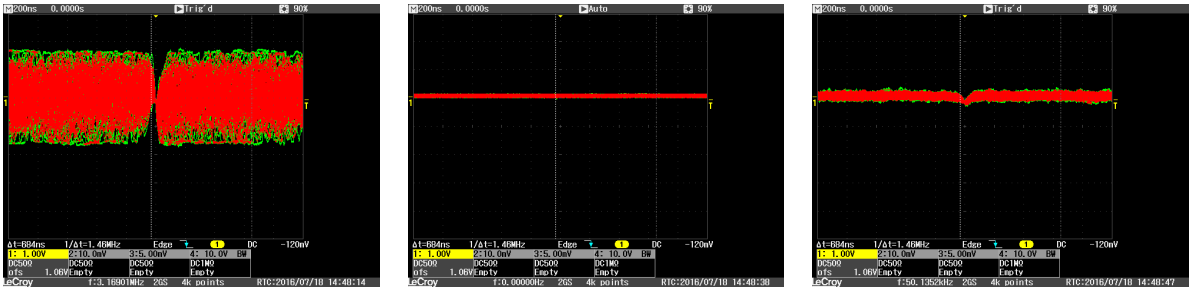

Figure 4.4.: Left: Screenshot of the oscilloscope signal measured in darkness, while the capping of FAMOUS is removed. **Mid**: Screenshot of the oscilloscope signal while the pixel is illuminated by the laser pointer. **Right**: Screenshot of the oscilloscope signal while an adjacent pixel ist illuminated. In all measurements, the voltage (div = 1 V) in dependence of the time (div = 200 ns) was recorded. Details in the text. Screenshots made by N. Höflich and B. Pestka.

4.3. Dark rate measurements

With all pixels wired, dark rate measurements are performed. In section 4.3.1, the measurement procedure is described. In section 4.3.2, the algorithm used to find and analyze the SiPM pulses in the oscilloscope's traces is explained. The analysis of the resulting finger spectra is done in section 4.3.3.

4.3.1. Measurement procedure

The pixels wired are connected one by one via an amplifier board to the oscilloscope as described in section 4.1. The FAMOUS power supply unit is turned on and an overvoltage of 1.4 V is set. The communication with the oscilloscope is done via Ethernet. A sampling rate of 1 GSa/s is implemented. In this way, one recorded SiPM trace consists of $5 \cdot 10^5$ samples with a time step width of 1 ns. For every pixel, two measurements with 100 traces each were recorded, corresponding to two times $100 \times 5 \cdot 10^5 = 5 \cdot 10^7$ samples or $5 \cdot 10^7$ ns = 0.05 s of data. As the thermal noise rate is approximately 1 MHz, about several tenthousand SiPM pulses should be measured in each of the two measurements. This guarantees a sufficient statistics for the analysis of the pulses.
In figure 4.5, an exemplary screenshot of a recorded trace is shown. The amplified SiPM signals can be seen as down-pointing spikes. Several different levels of peak heights can be identified, corresponding to the 1 p.e. peaks, 2 p.e. peaks and so on.

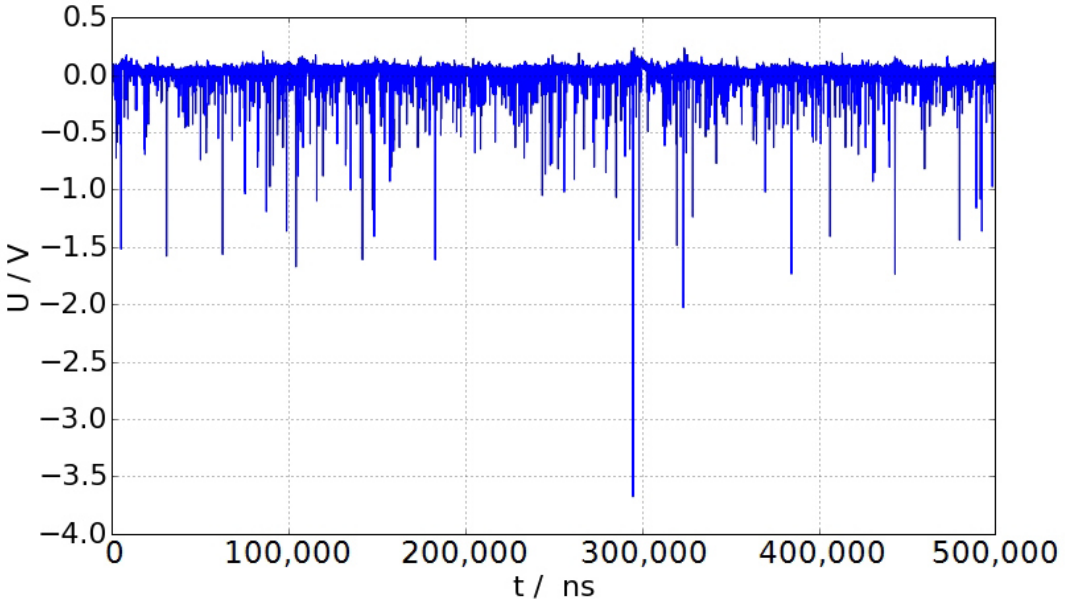

Figure 4.5.: Plot of one SiPM trace. The pulses were amplified and measured with the oscilloscope, as explained before. The voltage is recorded as a function of time. The sampling rate is 1 GSa/s, equal to $5 \cdot 10^5$ recorded samples with a time step width of 1 ns. The voltage division is 500 mV.

4.3.2. The signal extraction algorithm

To analyze the recorded SiPM pulses, it is necessary to extract them from the SiPM traces. Due to the high number of pulses, a signal extraction algorithm is needed. In short, the algorithm has to detect the SiPM pulses, integrate over them and subtract the baseline.
The algorithm used is written in python and consists of three main parts.

The first part is the flattening of the SiPM trace. The presented approach was also used in the bachelor thesis of C. Günther [20]. For the flattening, the average of always five neighboring values in the trace is calculated. This reduces the fluctuation of the trace due to baseline fluctuations. The so calculated flattened trace can be used to find the peak positions. It can not be used for the further analysis of the pulses, because the averaging falsifies the pulse integral and can also change the slope of the pulses.

The second part is the peakfinder. The basic algorithm was written by M. Duarte and is available online [31]. The algorithm uses the value of a point compared to the points around as criterium for a peak. Both hills and valleys can be detected. As the SiPM pulses are negative, it was searched for valleys in the flattened trace. A position in the trace is detected as a peak position, if the corresponding value is lower than the values of the points around. To filter the detected peaks, a minimum peak height and a minimum peak distance can be set in the algorithm. The minimum peak height was set to 0.02 V, but this value is not relevant for the analysis, as a similar filter criterium was implemented in the analysis program at a later time. The minimum peak distance was chosen to 20 ns. This is necessary, because even the SiPM pulses in the flattened trace are not perfectly sharp. If no minimum peak distance is set, the same peak could be detected several times.

The detected peak positions in the flattened trace were translated to the unflattened trace. Unfortunately, as the peakfinder only uses the peak height for peak detection, not only SiPM pulses, but also electronic noise is detected. One source of electronic noise with a pulse height similar to the SiPM pulses is the socalled “Hallenrauschen”. In the building where the laboratory with the FAMOUS telescope is located exists a characteristic electronic noise in form of several

oscillations. The reason for this noise is unknown and it occurs with no stable frequency and amplitude. Fortunately, the absolute value of the slope of the SiPM pulse is higher than of the electronic noise signal.

Therefore, a filter was implemented in the signal extraction algorithm, similar to the filter used by C. Günther in his bachelor thesis [20] . If a peak should be counted as a SiPM pulse, it has to have a negative value and a minimum slope. To calculate the slope, the recorded voltage at the peak position in the unflattened trace is compared to the voltage 20 ns before the peak. A similar criterium is applied on the flattened trace. If the absolute value of the difference in both traces is larger than 0.03 V, the peak is counted as a SiPM pulse.
Figure 4.6 shows exemplary which pulses are detected by the peakfinder (black diamonds) and which pulses are then counted as SiPM pulses (red points).

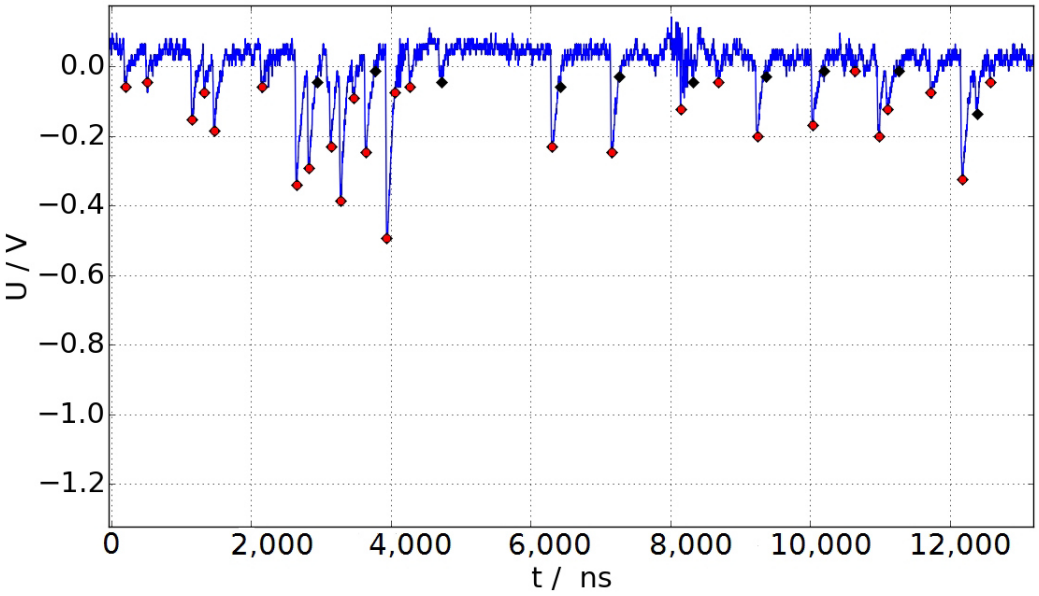

Figure 4.6.: Comparison of the peaks detected by the initial peakfinder (black diamonds) and the peaks finally counted as SiPM pulses (red points). The peak positions in the unflattened trace are shown. The SiPM trace was measured with the central pixel of the FAMOUS telescope. It can be seen that the initial peakfinder often detects extra peaks on the rising edge of the SiPM pulses. These peaks are filtered out by the other criterias of the signal extraction algorithm. Nevertheless, the filter makes some mistakes. Sometimes, small SiPM pulses are not detected and electronic noise is misidentified.

The third part of the signal extraction algorithm is the integration over the detected SiPM pulses. For this, the unflattened trace has to be used, as explained before. All voltage values from 20 ns before the detected pulse minimum to 20 ns after the minimum are added. The resulting value is then the pulse integral.

Because of the baseline fluctuation, it is necessay to subtract the baseline from the integral. For this, the voltage values from 30 ns to 20 ns left from the detected pulse minimum are added. The resulting, corrected pulse integral I_{corr} can then be calculated like this:

$$I_{\mathrm{corr}} = I - I_{\mathrm{baseline}} \cdot \frac{\Delta t_{\mathrm{pulse}}}{\Delta t_{\mathrm{baseline}}}\,, \tag{4.1}$$

with the pulse integral I, the baseline integral I_{baseline}, the pulse integration sector $\Delta t_{\mathrm{pulse}}$ and the baseline integration sector $\Delta t_{\mathrm{baseline}}$. The corrected integral is calculated for all detected peaks in all traces and saved in ASCII-files. Thus, two ASCII-files are produced for each pixel,

one for every measurement with the pixel.
Figure 4.7 shows exemplary the integration sector for the pulses.

The calculation of the baseline at the left side has the advantage that the SiPM pulse's slope is higher on this side. Because of this, the baseline can be calculated closer to the pulse minimum and is less falsified by the SiPM pulse tail. The disadvantage is that afterpulses can not be evaluated correctly with the chosen integration method. Instead of the baseline, a part of the first SiPM pulse would be subtracted. This falsifies the resulting integral. As the afterpulse is typically smaller than the first SiPM pulse, the resulting integral can even get the wrong sign, as can be seen in the next section.

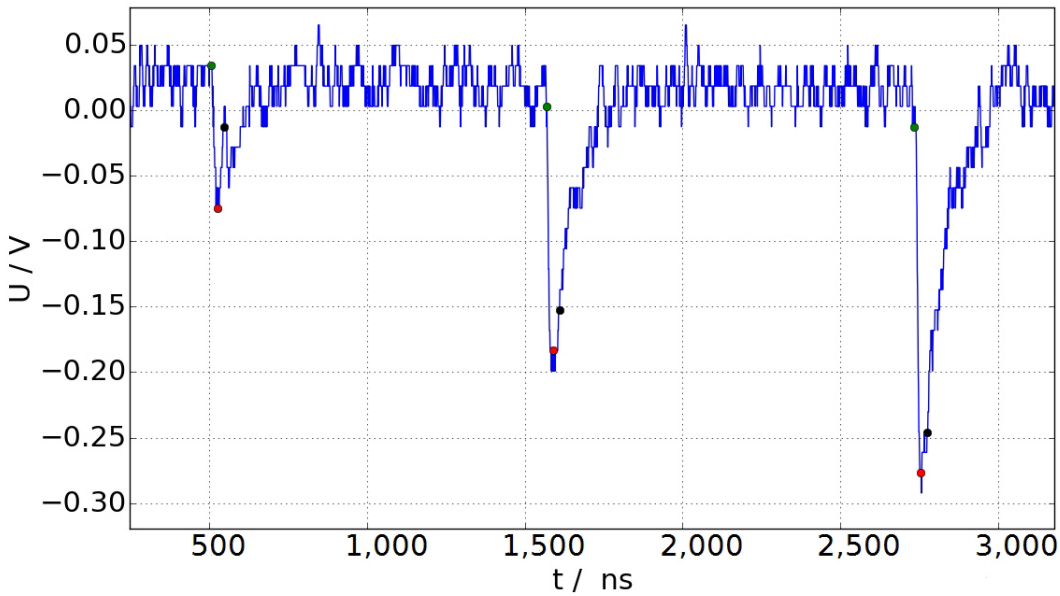

Figure 4.7.: Integration limits for the pulses. The red point marks the pulse minimum. The green points mark the left integration limits 20 ns left from the pulse minimum. The black points mark the right integration limits 20 ns right from the minimum. The unflattened trace of a measurement with the central pixel of the FAMOUS telescope is shown.

4.3.3. Analysis of the finger spectra

As described before, two measurements were performed for each wired pixel (i.e. each connected SiPM). All measurements were evaluated individually. This takes into account, that the different SiPMs may have variating properties. Additionally, it can be proven that the measurement- and analysis methods create stable results. The results of the two measurements with the same pixel should be compatible within their error limits.
As there are 20 analyzed FAMOUS SiPMs, it is not possible to show the results for every SiPM. All following plots were done with the data from the measurements with pixel 31, as this pixel lies in the middle of the FAMOUS camera. In the appendix, a table with the most important properties of all pixels can be found.

For the analysis, the calculated corrected pulse integrals are first multiplied with -1 and then filled into a histogram. In total, two histograms for each pixel are produced, each made of the pulses found in 100 SiPM traces.
In figure 4.8, an example for the resulting finger spectrum is shown (pixel 31, measurement 02). The peaks in the positive x range are the 1 to n p.e. peaks. The presumable reason for the smaller peak in the negative range are detected afterpulses. As explained in the last section, the corrected integral over these pulses is falsified because of the baseline correction method and will

have the wrong sign. Also, the signal extraction algorithm misidentifies some electronic noise signals as SiPM pulses despite the implemented filters. This also leads to additional structures in the spectrum. The electronic noise background also causes a widening of the fingers, as explained in [32].

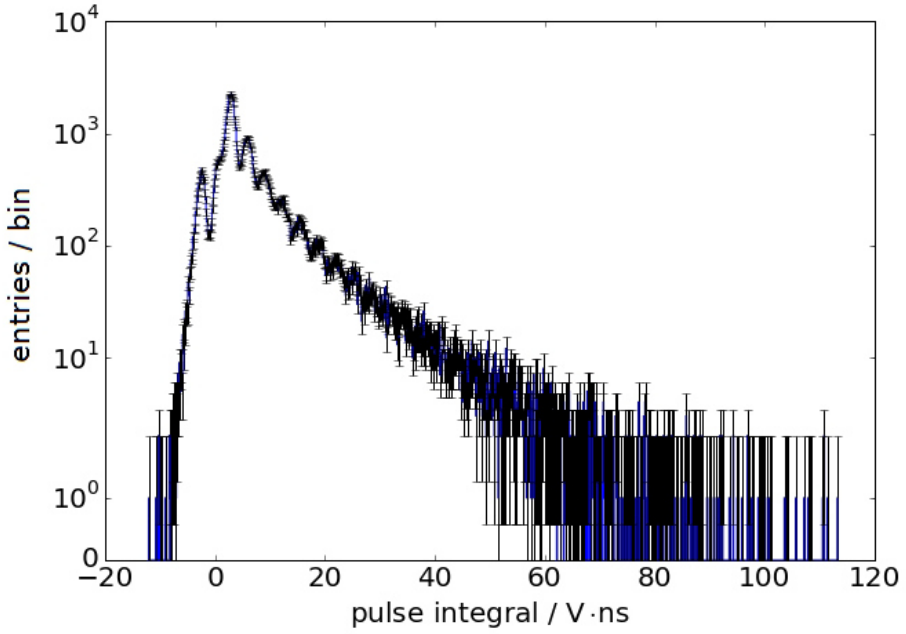

Figure 4.8.: Complete Finger spectrum with 96,117 entries of measurement 02 , pixel 31 . The absolute frequency ("Entries") of different pulse integrals (unit: $\mathrm{V} \cdot \mathrm{ns}$) is plotted. The histogram consists of 1024 bins in a range of approx. $125\,\mathrm{V} \cdot \mathrm{ns}$. The error on the bin height is the Poissonian error. The peaks in the positive range are identified as the 1 p.e. to n p.e. fingers. The presumable reason for the smaller peak in the negative range are several detected afterpulses and electronic noise, as explained in the text. Made by N. Höflich and B. Pestka.

The finger spectrum contains information about many interesting quantities of the SiPMs. For example,the peak distance is equal to the "size" of the 1 p.e. signal. If the amplification factor of the amplifier is known, the charge produced during the avalanche in the SiPM can be calculated. Therefore, the peak distance is called *gain* from now on. The relative peak height contains information about the crosstalk probability.
The analysis of the finger spectrum is done with two different methods. The first one is the fit of single gaussian functions to the peaks in the spectrum. With this method, the gain of the SiPMs is estimated. The second method is the FACT spectrum fit, which is used for the determination of the gain and the crosstalk probability.

4.3.3.1. Fit of single gaussian functions

The simplest method to calculate the gain is the fit of single gaussian functions to the fingers in the spectrum. This can be done as the pulse integrals are normally distributed around the p.e. position, if there is no systematic effect.

The fitted gaussian functions have the form:

$$f(x) = \frac{A}{\sqrt{2\pi\sigma^2}} \cdot exp\left(-\frac{(x-\mu)^2}{2\sigma^2}\right) \tag{4.2}$$

The amplitude A, the expectancy value μ and the standard deviation σ are optimized by the fit algorithm.

The functions were fitted to the first four fingers in the positive range, corresponding to the 1 p.e. to the 4 p.e. peak. Higher orders were not taken into account due to the small number of entries at these orders. As fit algorithm, the least-squares-fit is used. Figure 4.9 shows exemplary the fit of four single gaussians to the finger spectrum.

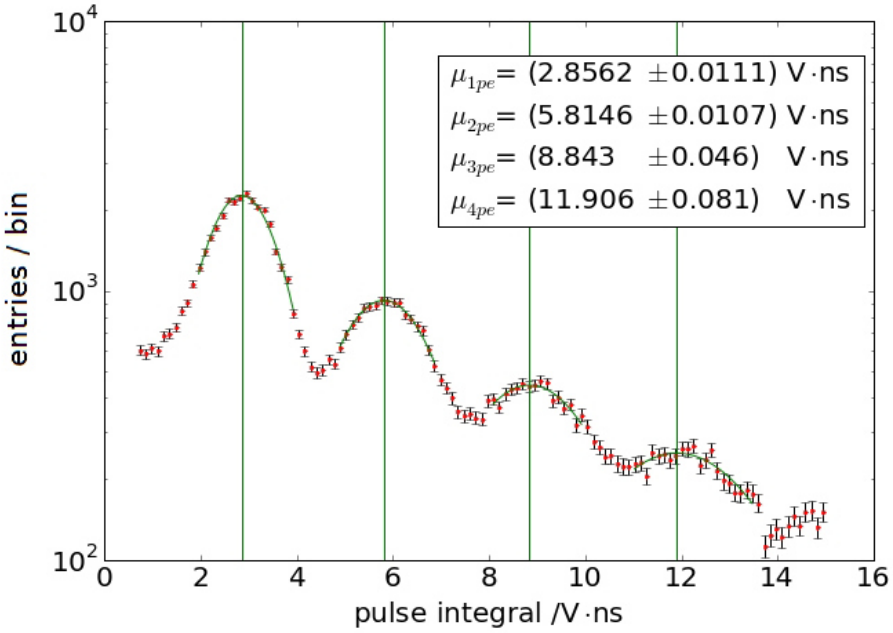

Figure 4.9.: Fit of four single gaussian functions to the first four p.e. peaks of the finger spectrum.The data is from the second measurement with pixel 31. Made by N. Höflich and B. Pestka.

The fit parameters are given in table 4.1.

	A	μ [V · ns]	σ [V · ns]	χ^2/dof
1 p.e.	4354 ± 62	2.856 ± 0.011	0.769 ± 0.015	37.31/14
2 p.e.	2359 ± 35	5.815 ± 0.011	1.022 ± 0.020	5.83/14
3 p.e.	1478 ± 99	8.843 ± 0.046	1.32 ± 0.10	12.79/13
4 p.e.	1059 ± 81	11.901 ± 0.081	1.69 ± 0.15	17.60/18

Table 4.1.: The parameters of the four fitted single Gaussians. It can be seen that expecially the errors on the standard deviation increase for higher p.e's. The reason is that the gaussian functions are less good to identify for higher p.e.'s.

To calculate the gain, the expectancy values of the gaussian functions are plotted against the number of the related peak. A linear regression is done. The slope of the fitted line is then the gain. In figure 4.10, an exemplary linear regression (again pixel 31 measurement 02) is shown. The corresponding residual plot is shown in figure 4.11. The gain is calculated to

$$gain = (2.977 \pm 0.020)\,\mathrm{V} \cdot \mathrm{ns}$$

The y-intercept is expected to be zero, as the baseline is subtracted. Nevertheless, the y-intercept is negative, as can be seen in figure 4.10. Additionally, a closer look to the 1 p.e. peak in figure 4.9 shows that the mean is smaller than expected based on the gain. The reason might be that not only the baseline, but also a small part of the falling edge of the SiPM pulse is subtracted so that the resulting integral is too small. As this problem would influence all pulses in the same way, it should not have an influence on the gain.

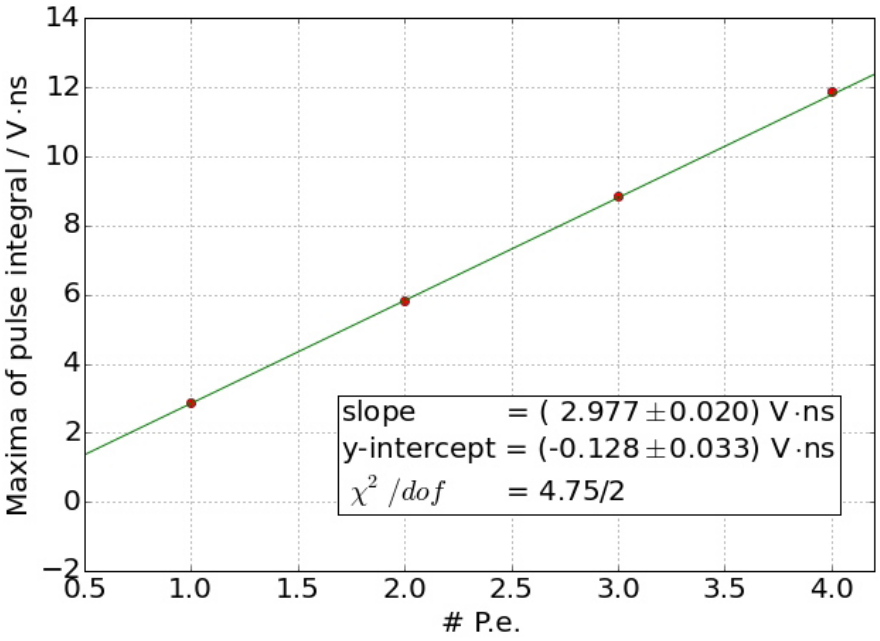

Figure 4.10.: Linear regression to calculate the gain. The expectancy value of the gaussian functions is plotted against the related p.e. The slope of the line is the gain. The y-intercept should be zero as the baseline was subtracted, but it is negative. A possible explanation is given in the text. Made by N. Höflich and B. Pestka.

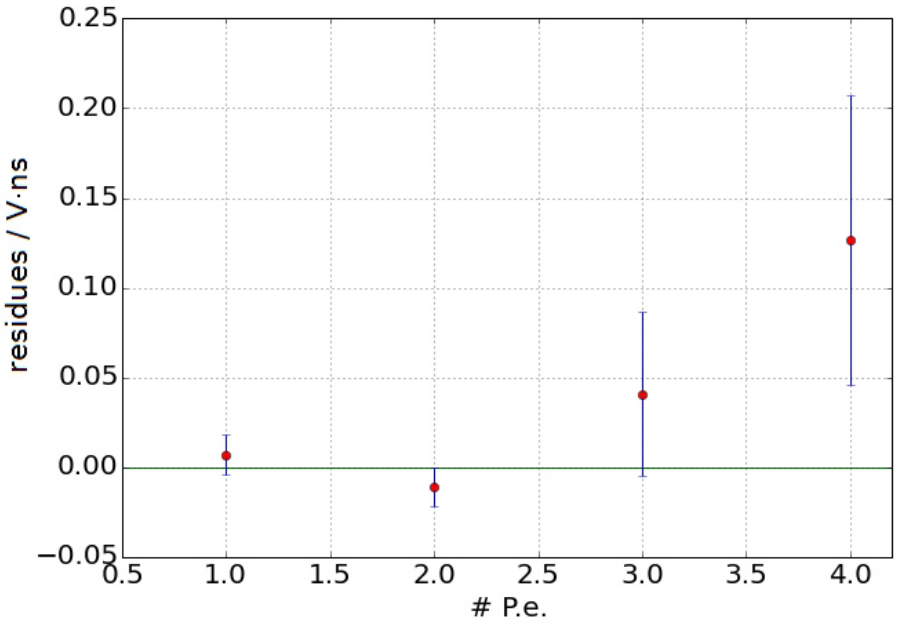

Figure 4.11.: Residual plot corresponding to figure 4.10. It can be seen that the calculated gain fits well for the 1 and 2 p.e. peak. For higher p.e. 's, the gain seems to be larger. The reason lies in the fitting method with four independent gaussian functions. The assumption of independency is not justifiable, especially not for higher p.e.'s. More information can be found in the text. Made by N. Höflich and B. Pestka.

In the residual graph (figure 4.11), it can be seen that the fitted line fits well for the 1 and 2 p.e. peak. For higher p.e.'s, the distance between the expectancy values seem to increase. This effect was found in many measurements. The main reason for this increase lies in the fit method. The peak maxima and peak forms in the finger spectrum are not independent from each other. As the width of the fingers increases for higher p.e.'s, the overlapping of neighboring peaks can not be ignored. Therefore, a fit of single gaussian functions is not suitable to describe a finger spectrum. The calculated gains are not more than an estimation and the calculated errors may be too small.
A better method for the analysis is the fitting of a sum of gaussian functions, or, even better, the FACT spectrum fit.

4.3.3.2. FACT spectrum fit

The FACT spectrum fit is developed by the FACT collaboration for the analysis of SiPM finger spectra. It uses a sum of n gaussian functions weighted with the modified Erlang distribution. Further information on the function can be found in the FACT paper [32] The fit function is given by:

$$f(x) = A_{1\mathrm{pe}} \cdot \sigma_1 \sum_{n=0}^{N} \frac{exp\left(-\frac{1}{2} \cdot \left(\frac{x-x_\mathrm{n}}{\sigma_\mathrm{n}}\right)^2\right)}{\sigma_\mathrm{n}} \cdot \frac{(n \cdot p_\mathrm{fit} \cdot e^{-p_\mathrm{fit}})^{n-1}}{(n-1)!^v} \tag{4.3}$$

The first part of the sum are the N gaussian functions. The parameters of these functions are given as follows: $A_{1\mathrm{pe}}$ is the amplitude of the 1 p.e. -peak. $x_\mathrm{n} = n \cdot gain + x_0$ is the position of the mean of the n-th gaussian function, shifted from the baseline by x_0. The standard deviation of the $n-$th gaussian function is given to

$$\sigma_\mathrm{n} = \sqrt{n \cdot \sigma_\mathrm{pe}^2 + \sigma_\mathrm{el}^2} \tag{4.4}$$

. σ_pe^2 describes the fluctuation of the produced charge in a cell breakdown, so $n \cdot \sigma_\mathrm{pe}^2$ describes the fluctuation of the total released charge. σ_el^2 is the fluctuation of the electronic noise. Both noise distributions are assumed to be Gaussian [32].
The second part of the sum is the modified Erlang distribution, with the Erlang parameter v. A simulation in the FACT paper [32] connects the parameter p_fit with the crosstalk probability p_xt. The result of the simulation is used in this thesis to calculate the crosstalk probability:

$$p_\mathrm{xt} = (0.723 \pm 0.004) \cdot \left(\frac{p_\mathrm{fit}}{0.440106 \pm 0.00010}\right)^{\frac{0.875 \pm 0.005}{0.9515 \pm 0.0020}} \tag{4.5}$$

In this bachelor thesis, the FACT function was fitted with a least squares algorithm to all pulse integral histograms of all pixels. Again, the results of pixel 31 are presented in the following. The results of the other pixels can be found in the appendix.
The fit was only performed for pulse integrals between $2.5\,\mathrm{V} \cdot \mathrm{ns}$ and $50\,\mathrm{V} \cdot \mathrm{ns}$. For higher values, only a few pulses were recorded. This causes very high statistical errors or, if a pulse integral was not measured at all, an error of zero due to the assumption of Poissonian errors. Furthermore, some pulses reached the end of the oscilloscope's range. For values smaller than $2.5\,\mathrm{V} \cdot \mathrm{ns}$, it can be seen that the 1 p.e. peak is a little bit assymetric. This may be caused by the signal extraction algorithm. Therefore, these values were ignored in the FACT fit.

As the FACT function has many adaptable parameters, it is necessary to give the fit algorithm starting values for the variables. For that, the single Gaussian functions can be used. As a guess for the gain, the gain from the linear regression was used. The shift from the baseline x_0 can be estimated by the mean of the 1 p.e. peak. σ_pe^2 and σ_el^2 can be estimated by the variances of the 1 p.e. and 2 p.e. peak using equation (4.4):

$$\sigma_\mathrm{1pe}^2 = \sigma_\mathrm{pe}^2 + \sigma_\mathrm{el}^2 \tag{4.6}$$

$$\sigma^2_{\mathrm{2pe}} = 2\sigma^2_{pe} + \sigma^2_{\mathrm{el}} \tag{4.7}$$

Solving these equations for σ^2_{pe} and σ^2_{el} leads to:

$$\sigma^2_{\mathrm{pe}} = \sigma^2_{\mathrm{2pe}} - \sigma^2_{\mathrm{1pe}} \tag{4.8}$$

$$\sigma^2_{\mathrm{el}} = 2\sigma^2_{\mathrm{1pe}} - \sigma^2_{\mathrm{2pe}} \tag{4.9}$$

The crosstalk probability is estimated with 45 %, which is approximately the ratio of the peak heights in the finger spectrum. Out of this value, an estimation for p_{fit} is calculated with the use of equation (4.5). The number N of fitted Gaussians is not varied automatically by the fit program, as it is an integer. Instead, N is manually varied, until the fit describes the data best.

In figure 4.12, the fit of the FACT function to the data of pixel 31, measurement 02, is presented. The sum in the FACT function (equation 4.3) goes up to $N = 16$. The corresponding residual plot can be found in figure 4.13.
The gain is calculated to:

$$gain = (3.117 \pm 0.012)\,\mathrm{V} \cdot \mathrm{ns}$$

The crosstalk probability p_{xt} is calculated from the parameter p_{fit} with equation (4.5) to:

$$p_{\mathrm{xt}} = 0.5144 \pm 0.0059$$

The error on the crosstalk probability is determined with gaussian error propagation.

To check this result, it can be compared to the results of the first measurement done with this pixel. In the first measurement, the gain was calculated to:

$$gain_{\mathrm{1.Meas..}} = (3.128 \pm 0.013)\,\mathrm{V} \cdot \mathrm{ns}$$

The crosstalk probability was determined to:

$$p_{\mathrm{xt,1.Meas.}} = 0.5173 \pm 0.0063$$

It can be seen that the values match within their error limits.
The values for the other pixels can be found in the appendix. A closer look on these results shows that the results of the two measurements for each pixel match well. Obviously, the measurement and analysis methods can produce stable results. Additionally, the gain of all pixels lies approximately between $3.1\,\mathrm{V} \cdot \mathrm{ns}$ and $3.2\,\mathrm{V} \cdot \mathrm{ns}$ and is therefor similar for all pixels. An exception is the blind pixel that has a little higher gain with $3.27\mathrm{V} \cdot \mathrm{ns}$. As the gains are similar, the overvoltage for each pixel is apparently nearly the same.

With approximately 50 %, the calculated crosstalk probability is very high compared to the 35 % declared by the manufacturer [25]. This overestimation is probably caused by random coincidences. As the SiPM is composed by a huge number of cells due to its large size, the probability that several cells produce thermal noise nearly at the same time (within the integration length) independently from each other is relatively high. The resulting signal would then be the same as for correlated noise.

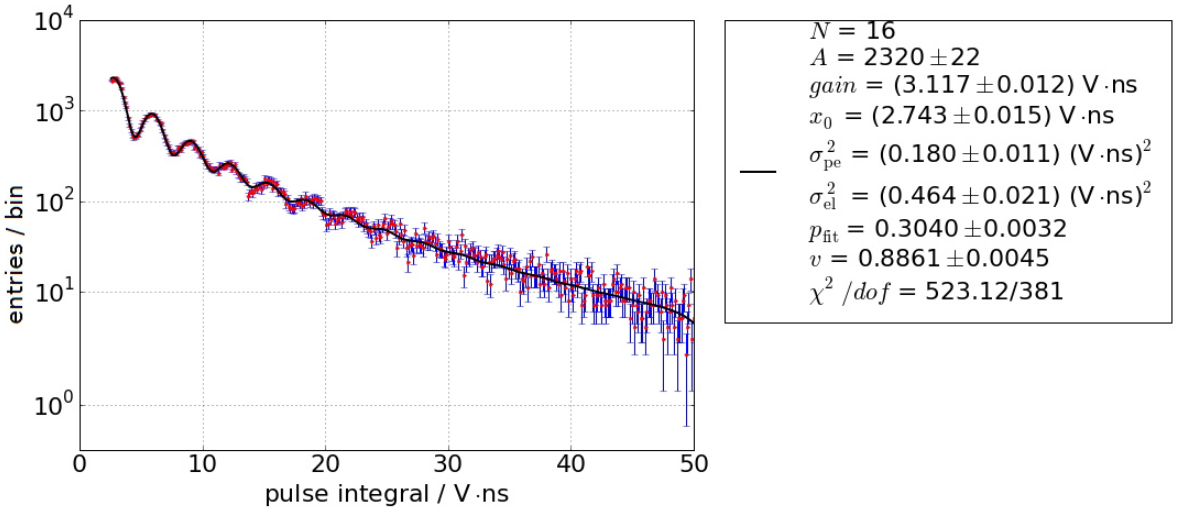

Figure 4.12.: Black line: Fit of the FACT function to the data of pixel 31, measurement 02. The sum in the FACT function goes up to $N = 16$. Red points: Histogram of pulse integrals with 67,947 entries. The fitting parameters can be found right from the plot. Made by N. Höflich and B. Pestka.

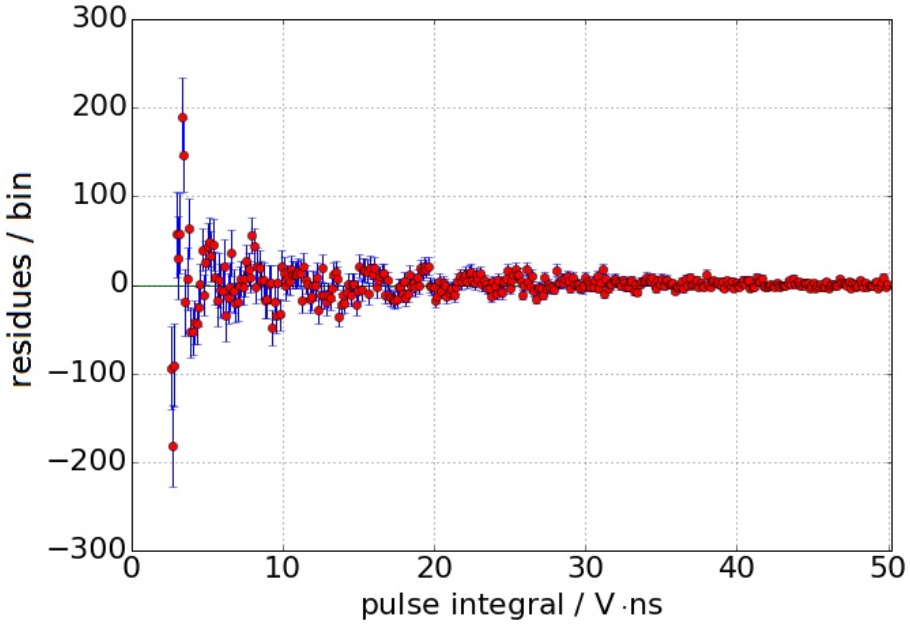

Figure 4.13.: Residual plot of the fit in figure 4.12. The residuals oscillate around zero for pulse integrals larger than approx. 10 V · ns. For very small pulse integrals, some data points does not match the fit well. Made by N. Höflich and B. Pestka.

A closer look on the fitted FACT function in figure 4.12 shows that the function describes the spectrum for the first peaks very well. Up to higher p.e.'s, two problems can be seen. First, the measured peak height is larger than calculated. Additionally, the calculated peak distance seems to be a little bit too small. This behaviour can also be seen in the residual plot. For higher p.e.'s, the residuals oscillate around zero. This discrepancy is not only found in the presented measurement, but also in the others.
Because of this, the FACT function was fitted again, this time only to the first five p.e. peaks. The result can be seen in figure 4.14 . The function fits well in the middle, but does not match well at the end of the spectrum. The reason is that this part is already overlapped with the 6 p.e.

peak. Also, a discrepancy between the function and the data at the left end of the spectrum can be seen. The reason is the asymmetry of the first p.e. peak, as explained before. These effects lead to a larger χ^2/dof as for the fit done before. Nevertheless, the gain of $(3.114 \pm 0.015)\,\mathrm{V \cdot ns}$ and also the crosstalk probability $p_{\mathrm{xt}} = 0.517 \pm 0.012$ match the values of the fit to the larger part of the spectrum within the error limits.

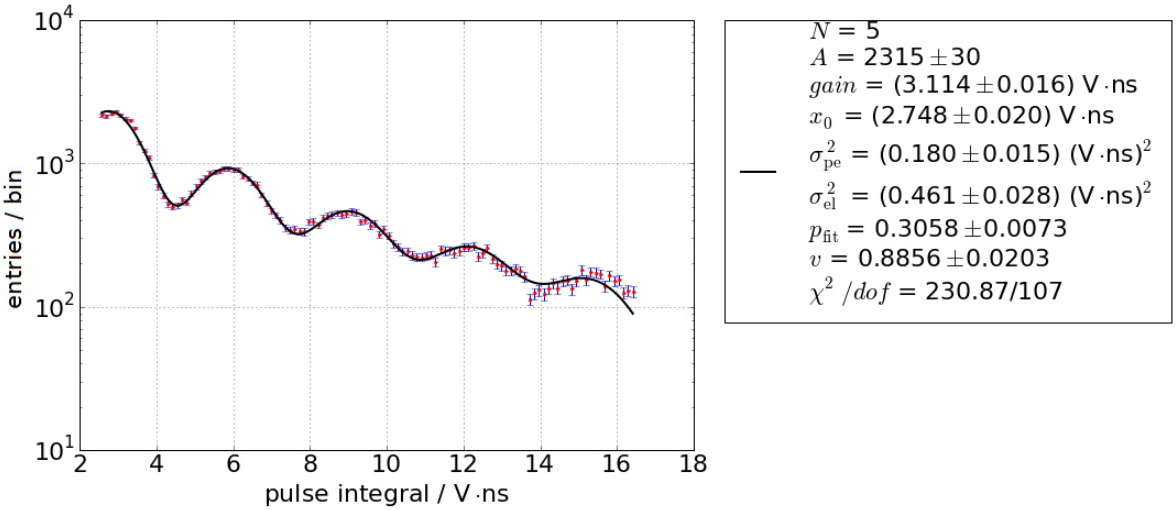

Figure 4.14.: Red points: Histogram of pulse heights with 58,811 entries. Black line: FACT function fit to first 5 p.e.'s. The function describes the main part of the data well, but does not match well at the end of the spectrum. The reason is that this part is influenced of the sixt p.e. peak. The calculated gain is very similar to the gain calculated with a larger part of the fingerspectrum. Made by N. Höflich and B. Pestka.

All in all, it was shown that gain and crosstalk probability of the SiPMs can be determined by the use of an oscilloscope. The gain of all pixels lies always between The interesting question is if it is possible to reproduce these results with the TARGET. In contrast to the oscilloscope, the TARGET is not a commercial data acquisition system, but only a prototype. Therefore it is expected that the result is less good, for example because of higher electronic noise. More concerning this question can be found in the next chapter.

5. Implementation of TARGET

In this chapter, the implementation of TARGET for the measurement of Cherenkov light of extensive air showers is described. The goal is to detect Cherenkov light successfully and that the number of detected photons on a pixel can be estimated.
After a short section about the basic measurement setup and the data recording, the baseline calibration, which is indispensable to successfully analyse the recorded data, is explained. Afterwards, the results of dark rate measurements for the gain calculation are presented. Finally, the measurements for Cherenkov light detection are analysed.

5.1. Basic measurement setup and data recording

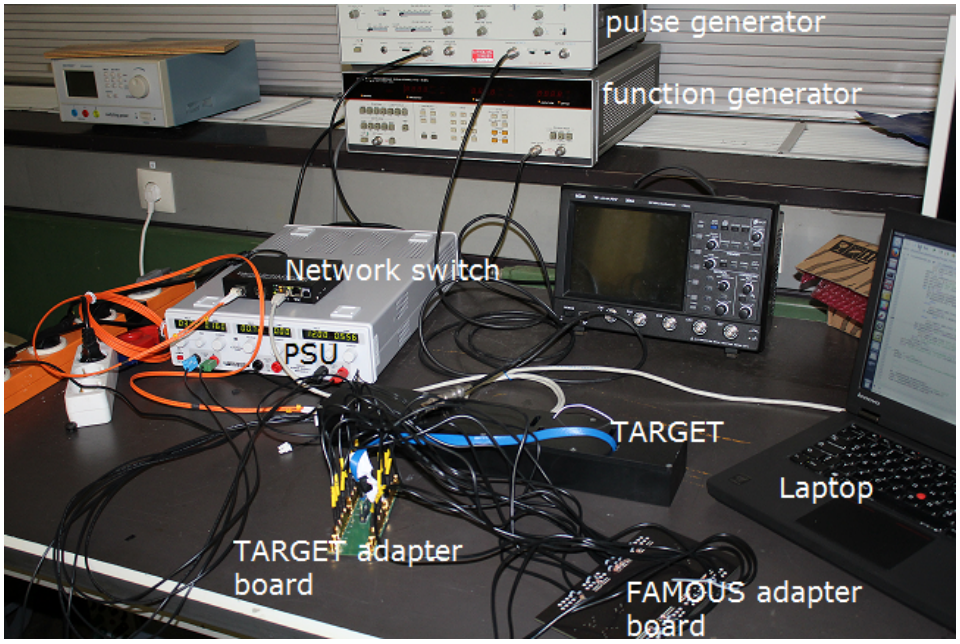

Figure 5.1.: Basic measurement setup (during the measurements in the following, the FAMOUS adapter board is of course connected to the SiPMs). The SiPMs of FAMOUS are connected via the FAMOUS adapter board and the TARGET adapter board to the TARGET module . The communication with TARGET is done via Ethernet. For that, the network switch is necessary. The voltage supply of TARGET is done by the laboratory PSU (*Rohde&Schwarz HM7042-5 triple power supply*). The TARGET needs a main voltage of 12 V and an additionally voltage of 3.3 V. The function generator triggers the pulse generator, which gives a trigger signal on the external trigger input of TARGET.

In figure 5.1, the basic measurement setup is shown. 16 out of 20 SMA cables of the FAMOUS' SiPMs are connected via the two adapter boards to one TARGET ASIC. For the operation, the TARGET module needs a main voltage of 12 V and additionally a voltage supply of 3.3 V [27], that are provided by a laboratory power supply unit (*Rohde&Schwarz HM7042-5 triple power supply*).
The communication with the module is done with the laptop via Ethernet. A network switch has to be used for that, as the TARGET does optical communication. The communication with

the FAMOUS PSU is done via Ethernet with a second laptop if necessary.
To trigger the data recording, a pulse generator (*Hewlett Packard 8082A pulse generator*) is used. Its output is connected to the trigger input of the TARGET module. As the minimum frequency of the pulse generator is too high for the measurement (1 kHz), the pulse generator is triggered externally by a function generator (*Hewlett Packard 8165A programmable signal source*). This allows a trigger rate of several tens of Hz. An oscilloscope (*LECROY WaveJet 354A*) is used to control the settings of the function generator and the pulse generator.

Data recording

To communicate with the TARGET module and record data, software can be found on the FAMOUS laptop. The data recording program, called "takedata.py", is written in python by E. Ganster and supplemented by B. Pestka and N. Höflich. It uses functions of the software packages created by the developers of TARGET. The program allows to do an adjustable number of measurements for an adjustable time. Furthermore, the trigger type and various trigger settings can be selected. The data is stored in .fits - files. To read these files, the internal software packages have to be used. Several plot and analysis programs exist, written by E. Ganster, B. Pestka and N. Höflich.

Further information on the software packages and the data recording can be found in [27]. A manual for the successful use of TARGET and the corresponding programs, written by B. Pestka and N. Höflich, can be found on the FAMOUS laptop.

5.2. Baseline calibration

The baseline describes the voltage values that are recorded even if no signal input is given to the TARGET.
In principle, the individual memory cells are capacitors in which the sampled voltage values can be stored. As these capacitors all have different properties, the baseline depends on the memory cell. Therefore, every memory cell has to be characterized individually.

In the following, a possible calibration method for all memory cells, based on the bachelor thesis of E.Ganster [27], is explained.
In contrast to E. Ganster's bachelor thesis, not the characterization of the baseline, but the development of a reliable calibration method for all memory cells has priority. This method will then be used for the measurements with FAMOUS.

To calibrate the whole baseline, it is necessary to measure multiple values for each memory cell. For that, the external trigger of TARGET can be used. As mentioned in section 3.3, the First Cell[1] changes from measurement to measurement, if this trigger type is used. If a sufficient number of measurements is recorded, each cell will be read out with approximately equal frequency. Thus, each cell can be calibrated with approximatly the same accuracy.
The calibration method is based on the calculation of the median for each memory cell individually, as also done in [27]. The advantage of the median over the mean is that it is less influenced by outliers. Furthermore, the median is an integer, just as the ADC counts.

The basic setup described in section 5.1 is used as measurement setup. As only the baseline shall be measured, the FAMOUS PSU is turned off.
The calibration measurements are done for two different voltage pedestals (*Vpeds*). The Vpeds can be set in DAC-counts (DAC = *D*igital to *A*nalog *C*onverter). The DAC has $2^{12} = 4096$ counts and a maximum voltage of 2500 mV. Therefore, the step size is given by $2.5\,\mathrm{V}/4096 \simeq 0.6\,\mathrm{mV}$

[1] Remember: The First Cell is the memory cell of the ringbuffer where the data readout starts.

[27]. A Vped of 100 DAC counts, equals $2.5\,\mathrm{V}/4096 \cdot 100 \simeq 61\,\mathrm{mV}$ and a Vped of 1500 DAC counts, equals $2.5\,\mathrm{V}/4096 \cdot 1500 \simeq 916\,\mathrm{mV}$, are used .
Each measurement is triggered by the pulse generator with a frequency of 10 Hz. For each voltage pedestal, 14 measurements over 30 s were recorded, corresponding to $14 \times 30\,\mathrm{s} \times 10\,\mathrm{Hz} = 4200$ recorded events in total.
As the position of the baseline depends on the temperature [27], it is taken care that the temperature stays constant during the measurement. Therefore, some heating measurements are done before the main measurement starts, until the TARGET reaches a constant operating temperature of $58\,^{\circ}\mathrm{C} - 62\,^{\circ}\mathrm{C}$ [27]. During the heating measurements, no data is recorded.

5.2.1. Characterization

In figure 5.2, two exemplary, consecutive events at a Vped of 100 DAC counts are shown[2].
Even if a Vped of 100 DAC counts is set, the baseline lies at about 300 ADC counts and therefore higher than expected. Obviously, the translation from the DAC to the ADC counts is not 1 to 1. More on this can be found in [27].
Both events in the plot have a very different First Cell. It can be seen that the baseline of the second event (First Cell 13720, in green) lies about 60 ADC counts above the baseline of the first event (in blue) with a First Cell of 1104. Obviously, the position of the baseline depends on the position in the ring buffer. More information concerning this can be found in [27].
For both events, the fluctuation of the baseline is approximately $30-40$ ADC counts. This makes clear that the baseline has to be calibrated if small signals shall be measured with the TARGET.

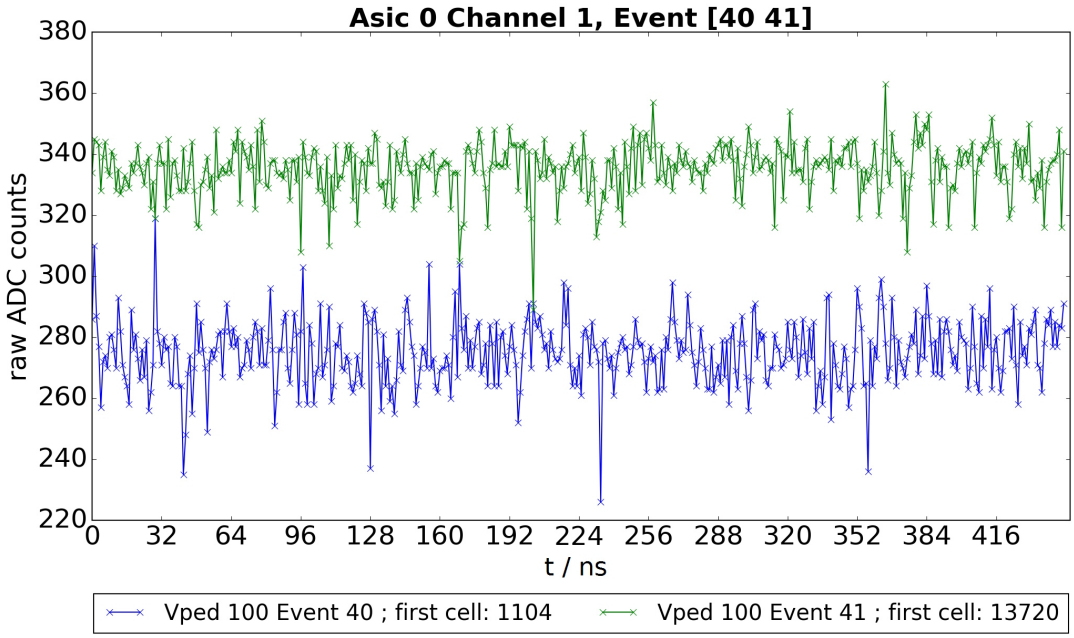

Figure 5.2.: Two exemplary, consecutive events at Vped 100. The trace was recorded with Channel 1 of the TARGET. Even if a Vped of 100 is set, the baseline lies at about 300 ADC counts.
The baseline of the first measurement with a First Cell of 1104 (in blue) lies about 60 ADC counts below the baseline of the second event with a First Cell of 13720 (in green). Furthermore, the fluctuation of the baseline is about $30 - 40$ ADC counts.

In figure 5.3, two exemplary events at a Vped of 1500 DAC counts are presented. Now the baselines lie at about $900 - 1,000$ ADC counts and therefore lower than expected.
Again, the baseline of the event with the higher First Cell (first Event, First Cell 11408, in blue)

[2] In the following, the Vped is always given in DAC counts. Therefore, the unit is not always mentioned.

lies above the baseline of the event with the lower First Cell (second Event, First Cell 824, in green).
Additionally, spikes downwards can be seen in constant distances of 32 ns. These spikes are also described in [27] and only occur for higher Vpeds. It is presumed that the reason for this effect is a mistake in the digitalization of the samples read out. Always one cell of a block in the buffer is digitized wrong. As the distance is always 32 memory cells, it seems like it is always the same cell number in each block [27]. A closer look to the position of the first spike shows that it depends on the event, respectively the First Cell of the event. The reason is, that the read out starts at a different point inside a memory block of 32 memory cells. Therefore, the distance to the cell number digitized wrong is different.

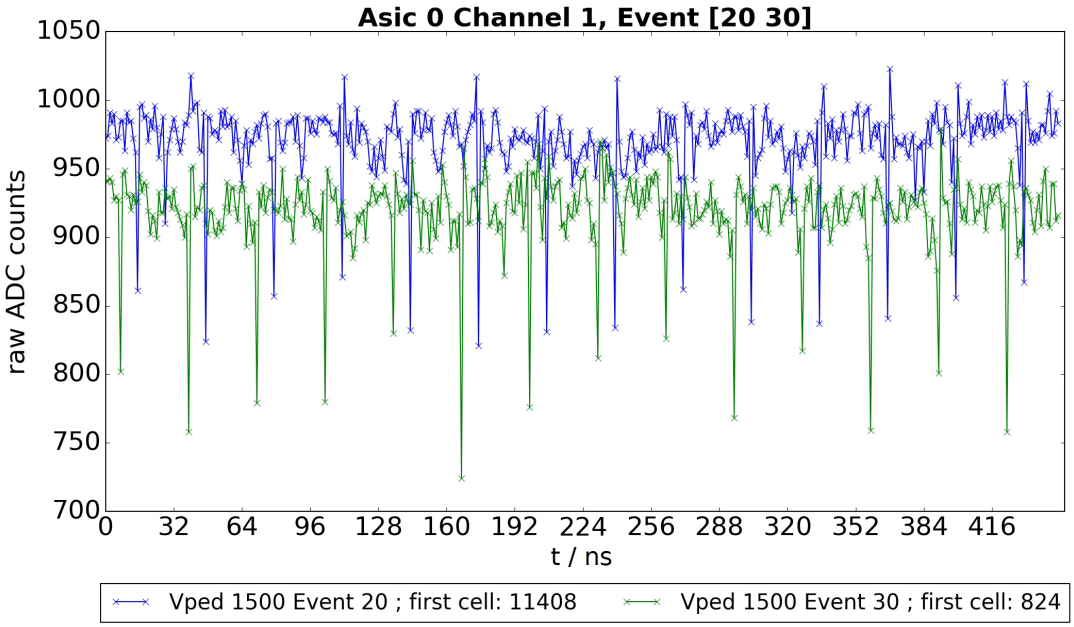

Figure 5.3.: Two exemplary events at Vped 1500. The baseline of the first event (in blue) with a First Cell of 11408 lies above the baseline of the second event (in green) with a baseline of 824. Furthermore, spikes downwards in a constant distance of 32 ns can be seen in both traces. Details in the text.

Another remarkable effect is that the First Cell of the events can always be divided by 8. Obviously, the data readout can only start at the 0th, 8th, 16th, 24th, ... cell in the ring buffer. Translated to the block structure of the buffer, the data readout can only start at the 0th, 8th, 16th or 24th cell of each memory block.

5.2.2. Calibration of the whole baseline

After the uncalibrated baseline was shown and discussed, now the calibration of the whole baseline will be explained.

As a start, the baseline calibration is done with the median of each cell. For that, all recorded samples are sorted to their corresponding memory cell in the ring buffer. Therefor, a program written by E. Ganster is used. The procedure is as follows: The First Cell of an event is read out. The following samples of this event are then sorted by the use of the First Cell into a list containing 16384 sublists . These sublists stand for the 16384 memory cells. This has to be done for each channel individually.
After the sorting, the median of every sublist, i.e. every single memory cell, is calculated. Like this, one gets an individual correction value for each cell.
To check the calibration, the so calculated baseline of the median values can be subtracted from

the baseline of a single measurement. This is shown in figure 5.4. A comparison between this plot and figure 5.2 shows that the fluctuation of the baseline does not become smaller for all samples due to the calibration. It seems like the calculated median does not fit to the data.

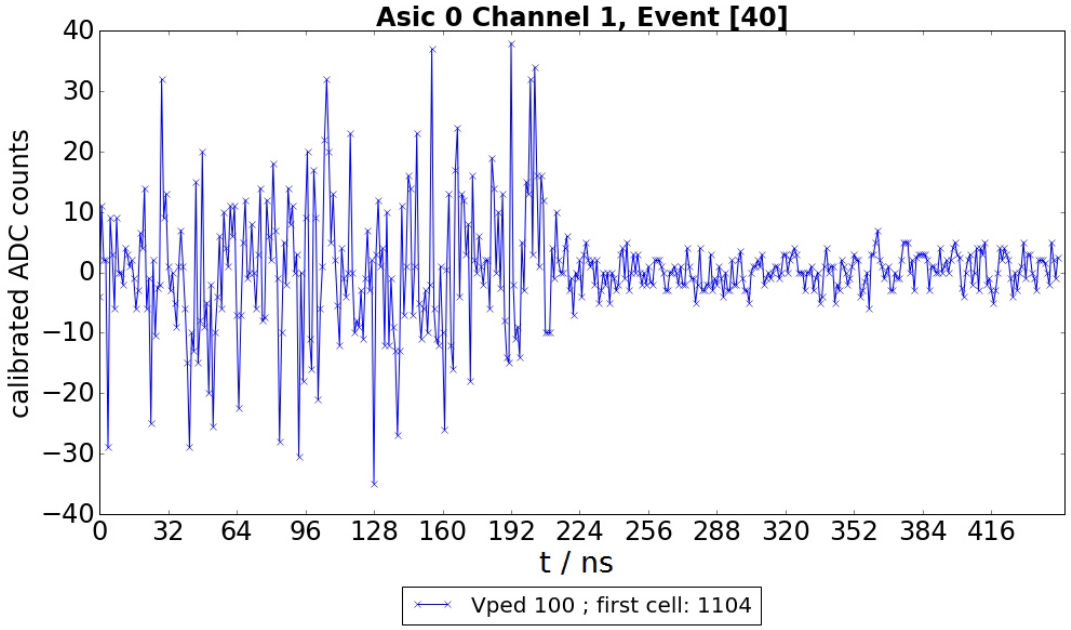

Figure 5.4.: The baseline of channel 1 at a Vped of 100, corrected by the median of the baseline. The plotted event is the same as in figure 5.2. In contrast to the expectation, the fluctuation of the baseline does not become smaller for all samples due to the calibration. Only in the right part of the trace, the fluctuation became significanty smaller. This indicates that the calculated median does not fit to the data.

Due to the insufficient results of the calibration, a closer look to the recorded memory cells is necessary. It is discovered that the values for the same memory cell does not fluctuate around one mean value, but around two different mean values. This is demonstrated in figure 5.5.
In the plot, the values of the baseline for Cell 1983 and Channel 1, recorded in many measurements, are plotted against the First Cells of the measurements. The Vped was set to 1500. Two populations of baseline values can be seen, one at approx. 820 ADC counts and one at approx. 730 ADC counts.

The sorting to the populations is not random. Which baseline value is recorded for Cell 1983 depends on the First Cell. A zigzag *structure of 32* can be seen. This means the following: If a positive integer x with $x < 32$ exists, for that $(First\,Cell - x)\%64 = 0$, the recorded baseline value for Cell 1983 belongs to the upper population. If a positive integer x with $x < 32$ exists, for that $(First\,Cell - x)\%32 = 0$ but $(First\,Cell - x)\%64 \neq 0$, the recorded baseline value for Cell 1983 belongs to the lower population. Reffered to the block structure of the buffer, the first case is equal to an even starting block number, and the second case to an odd number.
This *structure of 32* is found for all memory cells for all channels. Nevertheless, the distance between the two populations is not always as large as seen in figure 5.5. Sometimes, it amounts only a few ADC counts.

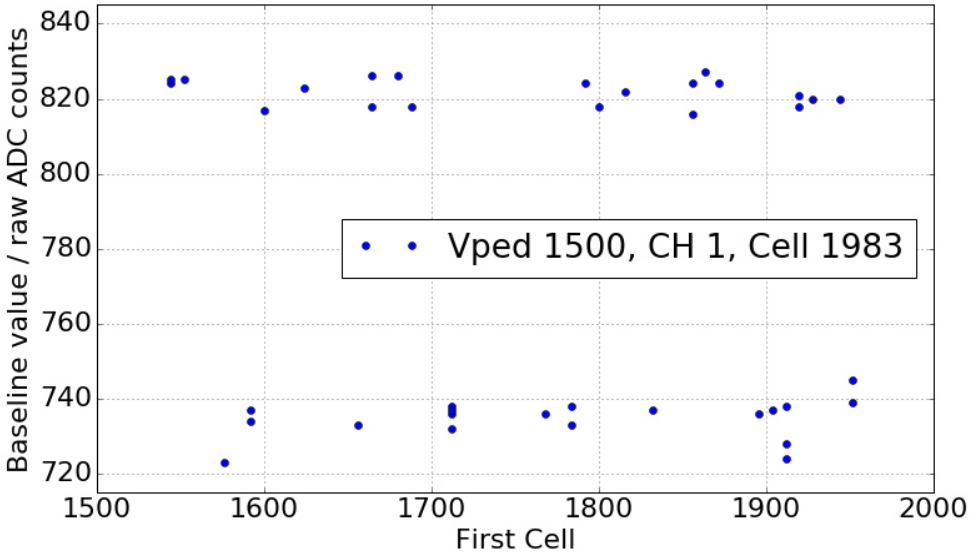

Figure 5.5.: The values of the baseline of one memory cell (cell 1983, channel 1), depending on the First Cell of the event in which the memory cell is read out. A Vped of 1500 DAC counts is used. Two populations of values can be seen, even though all these values were recorded for the same cell in the ring buffer in multiple measurements. A clear dependence on the First Cell can be seen. This dependence is explained in the text.

As the *structure of 32* can be found for all memory cells and channels, it can easily be considered in the calibration. Instead of one median, two medians are calculated for each memory cell, one for each population. If a measurement shall be corrected by the baseline, the First Cell of the measurement is read out. Depending on the First Cell, it is decided which median is subtracted. This procedure was implemented in the calibration programs by N. Höflich and can now be used for the baseline calibration. The sorting of the baseline values to the populations uses the divisibility of the First Cells by eight.
To check if this procedure is really suitable for the calibration, it is applied to a baseline measurement. The result for Vped 100 can be seen in figure 5.6. In the appendix, the result for a Vped of 1500 DAC counts is shown. Looking at the plot, it can be seen that the baseline fluctuates around zero. The fluctuation amounts to only a few ADC counts. From that, it can be concluded that the calibration considering the *structure of 32* is suitable.

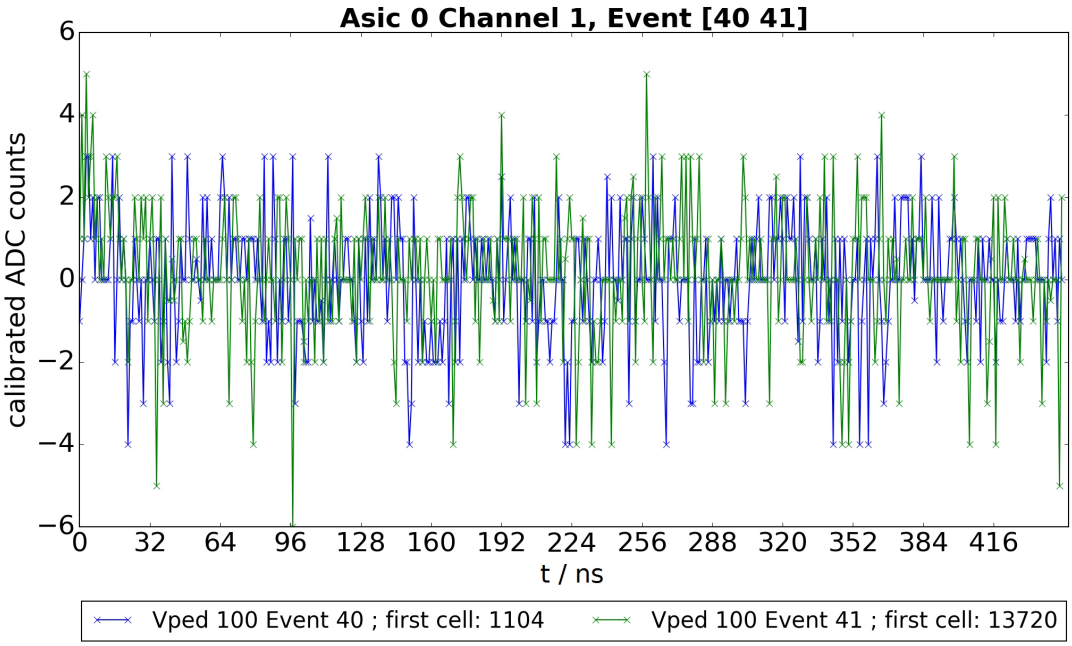

Figure 5.6.: Baseline corrected by the median of the baseline, considering the *structure of 32*. The presented events are the same as in figure 5.2. The fluctuation of the baseline is only a few ADC counts, in contrast to figure 5.4.

5.3. The Trigger Delay of TARGET

For all trigger types of the TARGET, a *Trigger Delay* can be set. With this delay, it can be controlled how many memory cells of the ring buffer shall be read out before the point the trigger signal is registered. The Trigger Delay can be set in ns.
To find the optimal setting for the Delay, a measurement series using the external trigger mode was done by B. Pestka. Thereby, the signal of a pulse generator was given both on the external trigger input and, damped by two 20 dB dampers, on a channel of the TARGET board. It was discovered that the trigger signal can not be seen in the recorded trace if the standard settings of the trigger delay are used. To see the signal completely in the trace, a Trigger Delay of more than 380 ns has to be set [29]. Because of this, a Trigger Delay of 424 ns is used in all measurements described in the following. This value is used as it leads to a First Cell divisible by 8. This is necessary for the use of the calibration method described in the last section. More information on the Trigger Delay can be found in [29].

5.4. Dark rate measurements

If a large SiPM pulse is measured with FAMOUS, the most interesting question is the amount of detected photons that caused this pulse. To calculate this, it is necessary to know the gain, respectively the size of the 1 p.e. signal. In the following, it is tried to determine this quantity with the use of the TARGET. As the TARGET's amplifiers shape incoming signals, the results of section 4.3.3 can not be used.
The measurements and the analysis are done in cooperation with B. Pestka.

5.4.1. Measurement setup and procedure

16 FAMOUS' SiPMs are connected to the TARGET as described in section 5.1. As the dark rate measurements are done after the measurement of Cherenkov light of air showers (described in section 5.5), the same layout, shown in figure 5.12, is used. The overvoltage is set to 1.4 V. Just as in chapter 4, the laboratory in which FAMOUS is placed is darkened and the capping of FAMOUS is put on.
The data recording is triggered externally with the use of the pulse generator (see sction 5.1) at a frequency of 30 Hz.
As TARGET settings, a Trigger Delay of 424 ns and a Vped of 1500 DAC – counts is used. The high Vped is chosen as it was also used for the measurement of Cherenkov light.
As it is tried to get a finger spectrum, 257 measurements over 20 s each are performed. This corresponds to $257 \times 20\,\mathrm{s} \times 30\,\mathrm{Hz} \simeq 154000$ recorded events with a length of 448 ns each. As the dark noise rate of the FAMOUS' SiPMs is approximately 1 MHz, it is expected to record about 70000 pulses. This guarantees a sufficient statistics.
Additionally, 25 calibration measurements are recorded. The calibration is done with the method described in section 5.2.

5.4.2. Identification of SiPM pulses

In figure 5.14, a SiPM pulse recorded with the TARGET is shown. The presented event is already corrected by the baseline with the method described in 5.2. The pulse is much higher than the baseline fluctuation. It can therefore be assumed that the pulse is a SiPM signal and not electronic noise.
It can be seen that the pulse is composed of two parts: First, a high positive part and second a smaller negative part. A comparison with figure 4.5 in chapter 4 shows two main properties: First, the pulse has the inverted sign. Second and more interesting, the pulse looks like the derivative of the pulses recorded with the oscilloscope. This is caused by the internal amplifiers of the TARGET module, as it was already investigated in [27] with the use of a rectangular pulse. The positive part of the TARGET SiPM pulse then corresponds to the left edge of the not derivated SiPM signal, the negative part corresponds to the right edge. As the right edge falls slower to zero, the negative part of the TARGET SiPM pulse is smaller than the positive part.

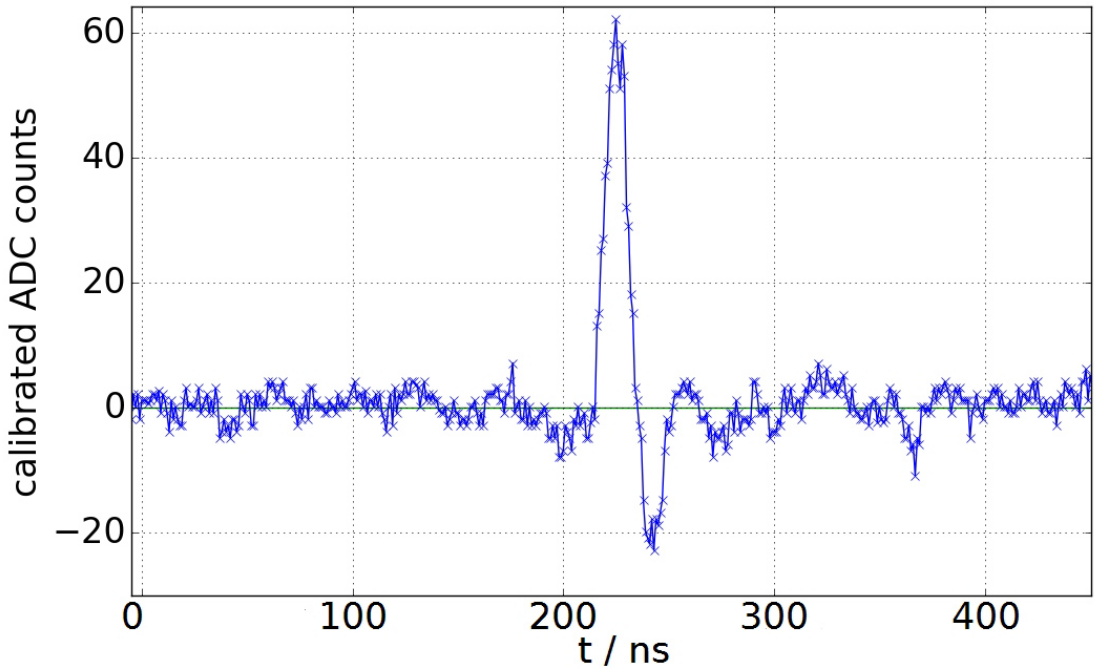

Figure 5.7.: Exemplary trace (Channel 11 equals pixel 46) with a recorded SiPM pulse. It can be seen that the pulse looks like the derivative of the input pulse, as can be seen by a comparison to the pulses measured with the oscilloscope in chapter 4. The length of the positive part of the pulse is about 20 ns. Details in the text.

5.4.3. Determination of the 1 p.e. signal

To determine the pulse integral of the 1 p.e. signal, a histogram of pulse integrals has to be made. For this, the pulses in the trace have to be found at first. Then the pulse integrals have to be calculated. These tasks are done by a signal extraction algorithm. After that, the histogram can be created.

The signal extraction algorithm used here consists of three parts.
First, all recorded events are corrected by the baseline with the calibration method explained in section 5.2. As the temperature of the TARGET varied due to the long measurement time, some measurements show a baseline shift to the positive or negative direction by a constant offset of a few ADC-counts. To correct this, for each event for each channel the median of the trace is calculated and subtracted.
The second part is the peakfinding. The peakfinding algorithm [31] is used for that. The minimum peak height is set to 13 calibrated ADC counts. This value lies about 5 ADC counts above the baseline fluctuation. The minimum peak distance is set to 200 ns, as the dark rate frequency is about 1 MHz.
In contrast to the measurements with the oscilloscope, no extra filter through the slope of the pulses can be implemented, as the slope is not significantly higher then the slope of baseline fluctuations or "Hallenrauschen".
At last, the pulse integrals are calculated. For that, it is integrated from 7 ns on the left to 8 ns on the right side of each detected peak maximum. This integration sector is approximately the positive range of the pulse.
The integrals are stored in a pickle-file and can then be histogramed.

In figure 5.8, the resulting histogram is shown. No fingers can be seen. Therefore, the histogram

does not allow a reliable determination of the 1 p.e. signal. The position of the histogram's maximum can not be taken as estimation for the 1 p.e. signal, as a minimum peak height is set. One can not be sure if this minimum peak height is smaller than the 1 p.e.pulse height and if therefore the peak in the spectrum is caused by these pulses.

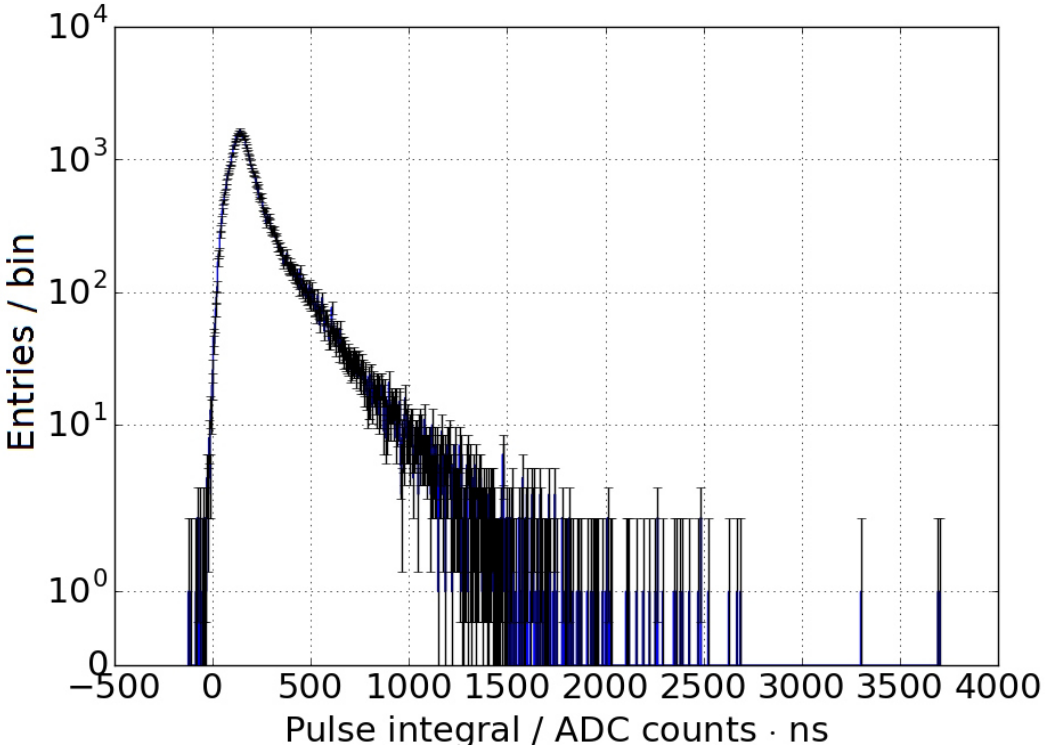

Figure 5.8.: Complete histogram of pulse integrals with 1024 bins. The scale of the y-axis is logarithmic. Unfortunately, no fingers can be seen in the spectrum. Only an exponential decay of the absolute frequency can be seen. Made by N. Höflich and B. Pestka.

As the histogram does not look as desired, the parameters of the signal extraction algorithm, namely the minimum peak height and distance and the integral limits, are changed. Furthermore, a baseline subtraction similar to the one used for the oscilloscope measurements is implemented. Unfortunately, all these adjustments do not leed to visible fingers in the histogram.

To at least approximate the pulse integral of the 1 p.e. pulses, several pulses with different heights are searched by hand in the traces. Thereby, discrete pulse heights can be found. The distance between these heights is always about 12 ADC counts. The smallest pulse than can be clearly distinguished from the baseline has a height of approx. 24 ADC counts and is therefore expected to be the 2 p.e. pulse.
A comparison of the pulse heights and pulse integrals allows then the estimation of the integral of 1 p.e. pulses. For that, 7 2 p.e. pulses and 7 3 p.e. pulses are searched and the pulse integral is calculated. Because of the fluctuations in the pulses, the error on the integral is estimated to 15 ADC counts · ns. The pulses are taken from two different channels. No significant difference in the pulse heights is found. As the gain of the SiPMs is always very similar, as shown in chapter 4, nothing different was expected. Therefore, the estimation of the pulse integral is not done for each channel separately. The weighted mean of the pulse integrals for 2 p.e. and 3 p.e. is calculated. The 2 p.e. and 3 p.e. signals are then calculated to:

$$S_{2\mathrm{pe}} = (220 \pm 6)\,\mathrm{ADC\,counts} \cdot \mathrm{ns}$$

$$S_{3\mathrm{pe}} = (343 \pm 6)\,\mathrm{ADC\,counts} \cdot \mathrm{ns}$$

The difference is then used as 1 p.e. signal estimation. With this, the 1 p.e.-integral is calculated to:

$$S_{1\mathrm{pe}} = (123 \pm 9)\,\mathrm{ADC\,counts} \cdot \mathrm{ns}$$

In figure 5.9, one example for a 2 p.e. and a 3 p.e. is shown. In figure 5.10, the relatively large fluctuation of the baseline can be seen. As the height of the 1 p.e. pulse is expected to be about half of the height of the 2 p.e. signal, these pulses are not much higher than the baseline. Therefore, the pulses are influenced by the calibration and the electronic noise, which makes the direct determination of the pulse integral very inaccurate. This is probably the reason for the lack of fingers in the histogram in figure 5.8.

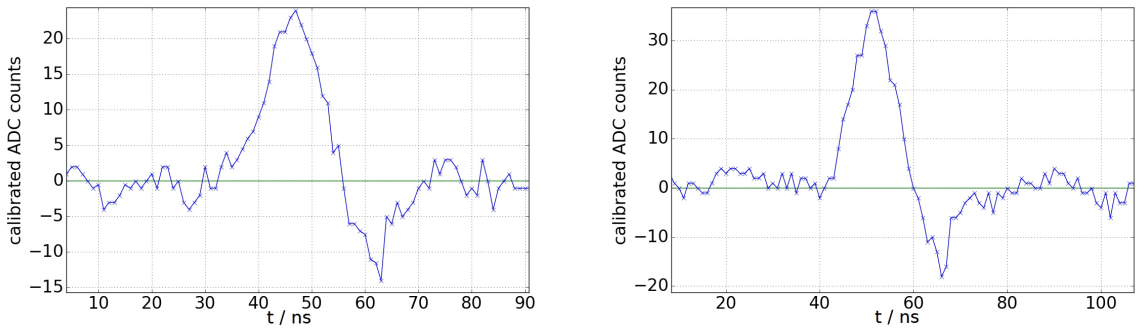

Figure 5.9.: Left: Exemplary zoom into a signal identified as 2 p.e. signal. **Right**: Exemplary zoom into a signal identified as 3 p.e. pulse.

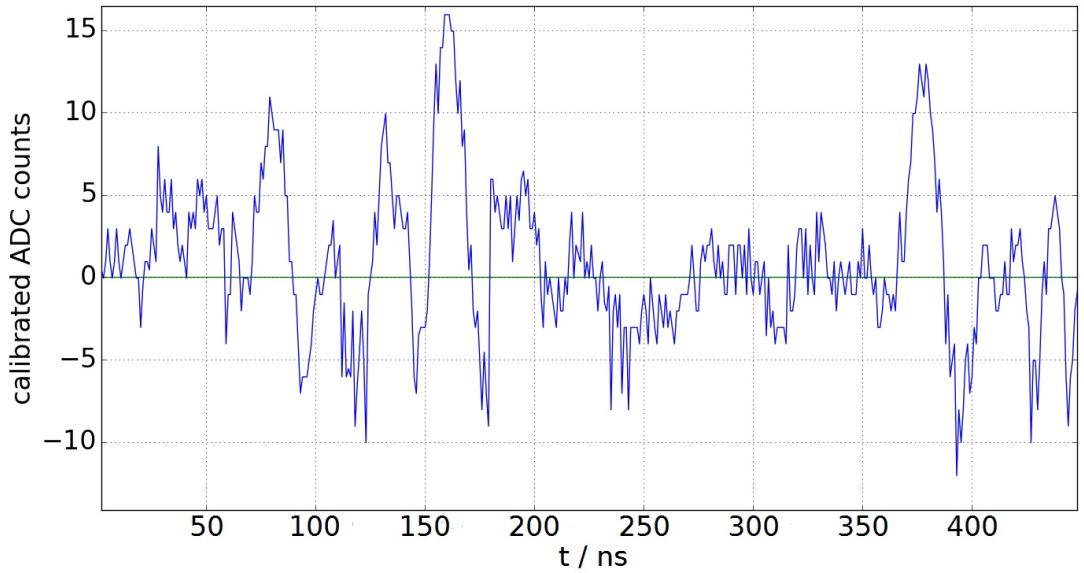

Figure 5.10.: Example for a high baseline fluctuation. In the right part of the trace, a possible 1 p.e. pulse can be seen. The pulse is not higher than the fluctuation in the left part of the plot. Aditionally, the structure of the fluctuation resembles the SiPM pulse.

To check the assignement of the pulse heights to the 2 p.e. and 3 p.e. pulse again, the rate of these pulses can be compared. The ratio between the rates of the 3 p.e. and the 2 p.e. pulses should be given by the crosstalk probability.
In chapter 4, the crosstalk probability was calculated to approximately 50 %. This value was however overestimated because of random coincidences due to the high number of cells and the

relatively long pulses ($\approx 100\,\mathrm{ns}$). As the SiPM pulses recorded with the TARGET are shaped by the internal preamplifiers and are therefore shorter (see e.g. figure 5.9), the rate of random coincidences is expeted to be smaller. Therefore, the ratio between the 3 p.e. and the 2 p.e. pulse is expected to be between 35 %, which is the crosstalk probability given by the manufacturer, and 50 %.
To determine the rate, it is searched in 100 measurements with about 600 events each, for pulses with a height between 21 ADC counts and 27 ADC counts for the 2 p.e. pulses and between 33 ADC counts and 39 ADC counts for the 3 p.e. pulses. This is done for every channel separately.
Afterwards, the ratio between the number of 3 p.e. and 2 p.e. pulses is calculated. In the appendix, a table with the number of detected pulses and the ratios can be found for each channel. Summarized, several thousand pulses are detected on every channel. The ratio of the rates is lies beween 38 % and 47 % and is therefore equal to the expected crosstalk probability. Therefore, it can be excluded that the difference between the pulse heights amounts to more than 1 p.e.because then, the ratio between the two analyzed pulse heights would be the square of the crosstalk probability and therefore below 25 %.

Even if the result for the 1 p.e. pulse integral is rather inaccurate with a relative error of more than 7 %, it allows an estimation of the size of large pulses. Like this, it can be determined if these pulses can be random or have to be caused by external light. More concerning this can be found in the next section.
For a more precise analysis, it is necessary to get a better estimation of the 1 p.e. pulse integral. For that, a finger spectrum has to be recorded. This may be possible with a lower Vped, as the baseline fluctuation is smaller then.

5.5. Measurement of Cherenkov light of air showers

As the TARGET shall be used as data acquisition for the FAMOUS telescope, it has to be proven that the use of the TARGET allows the detection of air showers.
Even if FAMOUS is constructed for the detection of fluorescence light, it is tried to measure Cherenkov light of air showers in this thesis. The reason is that the night sky brightness in Aachen is too high for an adequate fluorescence light detection rate. The detection rate of Cherenkov light is expected to be much higher. Also, as explained in section 2.3, the Cherenkov light is a light flash with a length of only a few nanoseconds. As the air shower is very extended in the horizontal direction, the Cherenkov light should be measured by more than one pixel of the FAMOUS camera. Therefore, it can be searched for large signals occuring in coincidence on several pixels in the recorded data.

5.5.1. The measurement setup and procedure

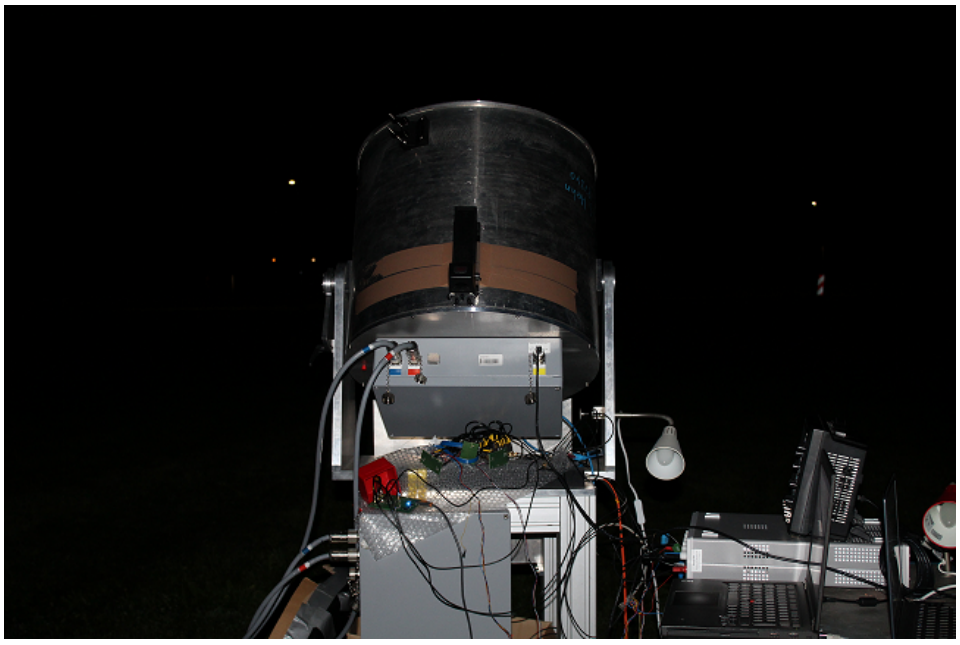

Figure 5.11.: Photography of the measurement. The FAMOUS telescope is placed on a meadow in front of the Physikzentrum, RWTH Aachen university. The measurement is done in a cloudless night by N. Höflich, B. Pestka and J. Schumacher.

To increase the detection rate, the amount of background light reaching the camera should be reduced as much as possible. Therefore, the measurement series is done in a cloudless night (in the night of 24.08.2016 to 25.08.2016, between 1:15 am and 2:40 am) on a meadow in front of the Physikzentrum of the RWTH Aachen university (GPS coordinates: 50.78149° N, 6.047293° E). The lens of the telescope is oriented west-facing and as vertical as possible to the sky to reduce the detection of light of surrounding buildings and street lighting.

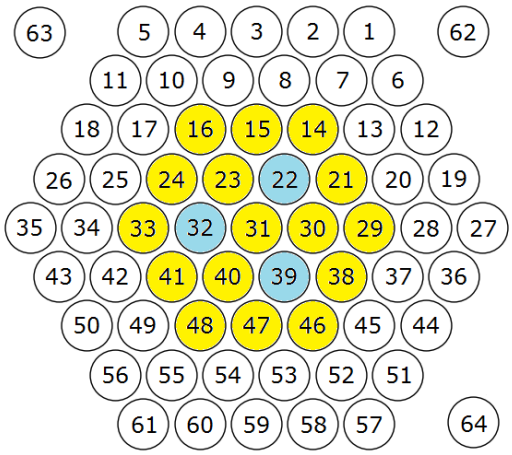

Figure 5.12.: Schematic depiction of the pixels connected to the TARGET (in yellow) and the three trigger pixels (in blue). It is triggered on the sum of the signals of the three trigger pixels. Details in the text.

16 pixels of the FAMOUS camera are connected to the TARGET as described in section 5.1. The overvoltage of the SiPMs is set to 1 V.
In figure 5.12, the layout can be seen. The yellow circles symbolize the connected pixels.

Trigger settings

The three blue circles (no. 22, 32, 39) symbolize the trigger pixels. As the self trigger does not work reliable at the moment, it has to be triggered externally. For that, it is triggered on the signals from the trigger pixels. The signal of each pixel is amplified by an amplifier board made by J. Schumacher. After that, the signals are given on a trigger board, made by J. Schumacher. Here, the signals are compared to an adjustable trigger threshold. If a signal exceeds the threshold, a trigger pulse ($>$2 V, $>$ 8 ns) is given on the external trigger input of the TARGET, starting the data recording.
It is taken care that the amplification factor for each pixel is similar to avoid different weighting of the trigger pixels. The trigger threshold is chosen to 0.93 V. With this value, the trigger frequency is about 0.4 Hz. The supply voltage for the amplifiers is provided by the power supply also used for the TARGET. The communication and the voltage supply of the trigger board is done via USB [29].
The three trigger pixels are not chosen at random. As can be seen in the layout, the pixels are arranged around the central pixel. Additionally, they are spread on the camera and surrounded by pixels connected to the TARGET. If Cherenkov light of an air shower hits one of the trigger pixels, it will probably also hit more than one pixel used for detection. As the trigger pixels are spread on the detection area, Cherenkov light arriving on different parts of the camera can trigger the data recording. Therefore, the detection rate is increased. Because the central pixel is surrounded by the trigger pixels, there is a high probability that an air shower triggering the data recording is recorded on the central pixel. This is advantageous as the Fresnel lens has the best imaging properties in the middle.

Measurement procedure

The measurement series is done by B. Pestka, J. Schumacher and N. Höflich. 14 measurements with a length of 5 min each are done. Unfortunately, there were problems with the data recording, so only 8 of the measurements can be used for the analysis.
For the baseline calibration, 18 measurements before and 15 measurements after the main measurements are recorded. Thereto, the connection of the SiPMs to the TARGET is interrupted and the trigger threshold is reduced to 0.83 V to get a higher trigger rate. It is taken care that

the temperature of the TARGET reached a nearly constant temperature before the calibration measurements or main measurements are started.
For all measurements, the Vped of the TARGET is set to 1500 DAC – counts. This value is chosen because of the shape of the SiPM pulses recorded with the TARGET. A pulse consists of a positive and a negative part compared to the baseline level. As large SiPM signals are expected, the negative part is also expected to be large. To make sure that this part of the pulse is completely visible in the trace, a relatively high Vped is chosen.
The trigger delay is set to 424 ns.
As the position of the baseline depends on the temperature, it is taken care that the temperature stays constant during the measurement. Therefore, some heating measurements are done before the main measurement starts, until the TARGET reaches a constant operating temperature of about 58 °C-62 °C depending on the ambient temperature. During the heating measurements, no data is recorded.

5.5.2. Analysis

In this section, it is tried to identify recorded events as air showers. It is started with a closer look on the recorded traces to identify large SiPM pulses. Afterwards, it is searched for coincidences in the data, that means large SiPM pulses on more than one channel at nearly the same time.

5.5.2.1. First look on the recorded traces

During the measurement series, altogether 1046 traces of a length of 448 ns each were recorded. Not all of them contain large SiPM pulses on one or several channels.
In figure 5.13, an exemplary trace is shown. The trace is already corrected by the baseline, using the data of the calibration measurements recorded before and after the main measurements and the method described in section 5.2. In the left part of the trace, between 32 ns and 64 ns, a large pulse can be seen. A comparison to the SiPM pulses shown in the last section shows that the shape is similar, but the pulse is about $100 - 200\times$ higher. Therefore, this pulse could be caused by Cherenkov light. To find this out, it has to be searched for coincidences.

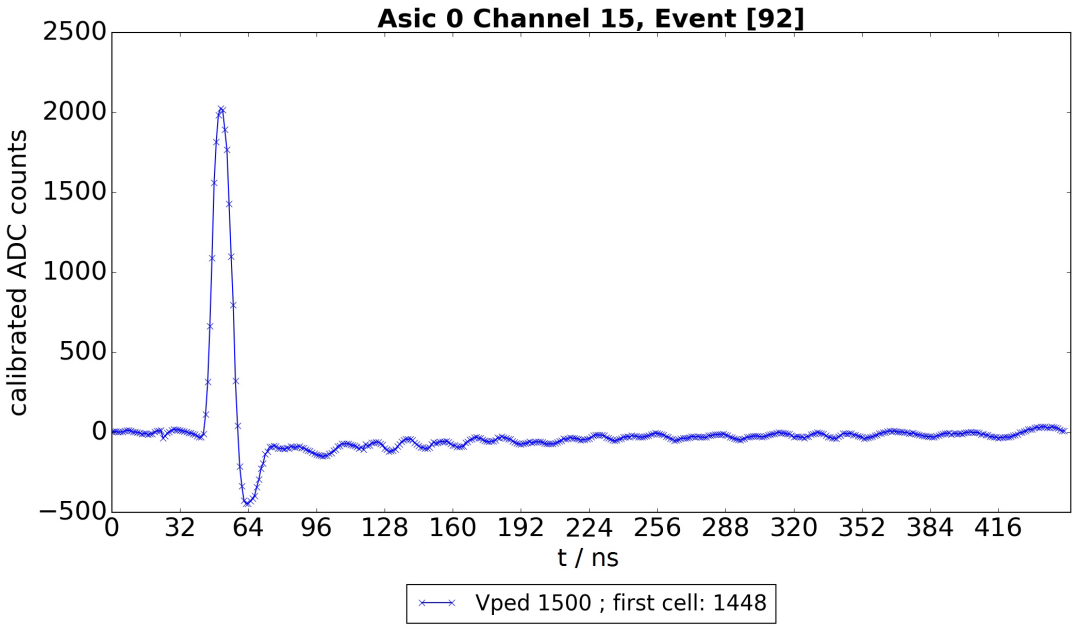

Figure 5.13.: Exemplary trace with a length of 448 ns. The trace is already corrected by the baseline using the method explained in section 5.2 and the calibration measurements recorded before and after the main measurements. Channel 15 of the TARGET corresponds to pixel 47. Plot made by N. Höflich and B. Pestka.

It has to be mentioned that not all pulses look as good as shown in figure 5.13. Pulses with a height of about 2500 calibrated ADC counts, respectively approx. 3500 raw ADC-counts, are cut off at the top, as can be seen in figure 5.14. A possible reason for this effect is that the preamplifiers of the TARGET module were saturating due to the large input signal.

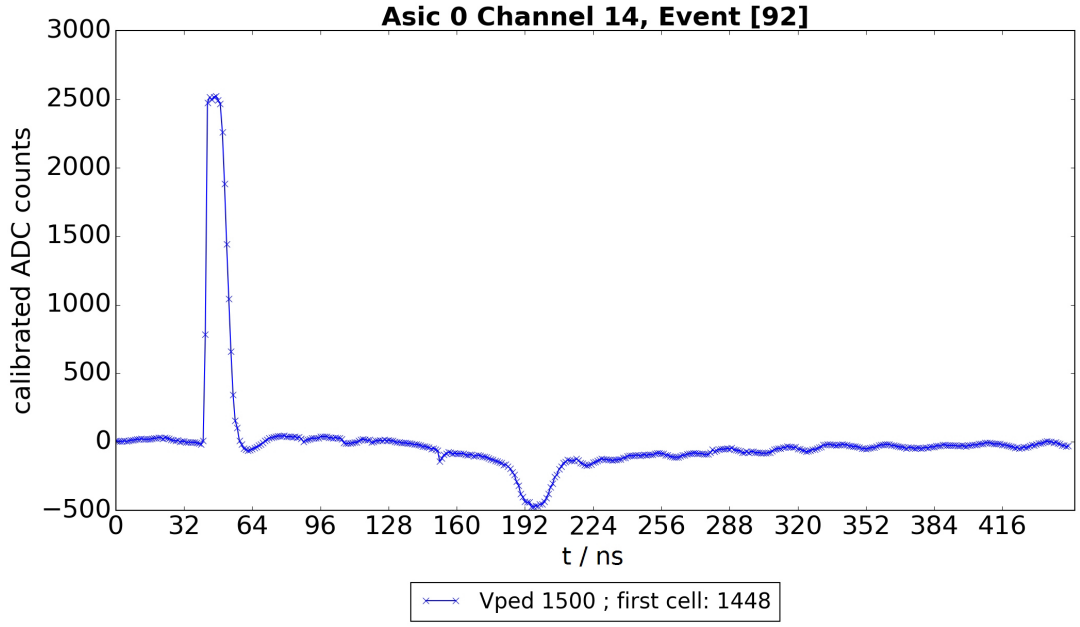

Figure 5.14.: Exemplary trace containing a pulse cut off at the top. The trace has a length of 448 ns. Channel 14 of the TARGET corresponds to pixel 41.
The pulse is probably cut off because of a saturation of the preamplifiers of TARGET due to a (too) large input signal.
This pulse is recorded in the same measurement, event and time as the pulse in figure 5.13. More information on coincidences like this can be found in the next section. Made by N. Höflich and B. Pestka.

In all traces with such a pulse, the drop of the SiPM pulse in the negative range directly after the spike in the positive range is missing. Instead, a drop in the trace about 150 ns later can be seen. This can also be explained with a saturation of the preamplifiers. As the input pulse is too large for the preamplifiers, not the whole pulse is shaped. Only the beginning and the end of the pulse can be handled by the preamplifiers. The visible spike in the positive range is therefore the beginning of the pulse, until the preamplifiers are saturating. The drop 150 ns later is caused by the end of the input pulse, when the preamplifiers are not saturating anymore.
Additionally, some channels have a drop in the trace exactly at the time a very high or cutted pulse is registered on another channel, as can be seen in figure 5.15. After that, a pulse looking like a delayed SiPM pulse is recorded. The reason for this effects is not known. Maybe the high pulse on one channel leads to a Vped reduction on some other channels. The delayed SiPM pulse may be caused by electronic crosstalk between the TARGET channels.

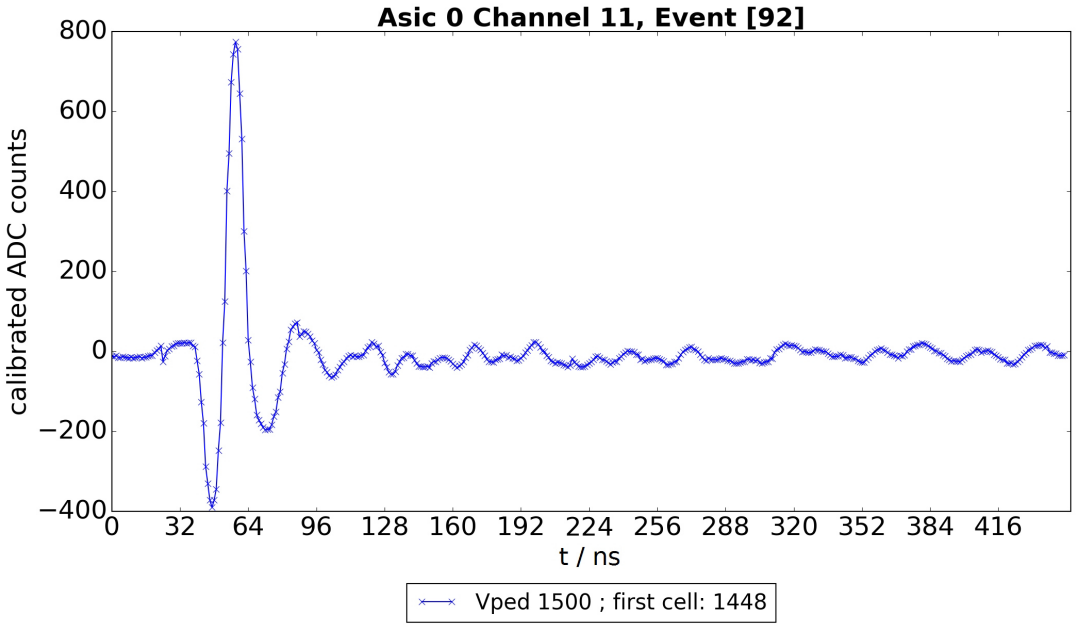

Figure 5.15.: Delayed SiPM pulse after a drop in the trace. The drop is registered in the moment another channel registers a very high pulse (order of magnitude: 2000 calibrated ADC counts). The plot shown here corresponds to the two figures above. Channel 11 of the TARGET corresponds to pixel 46. Made by N. Höflich and B. Pestka.

5.5.2.2. Search for coincidences

To find coincidences in the data, the calibrated traces of all events of one measurement are put in a row for each channel individually. To find the position of large pulses in the trace, the peakfinding algorithm [31] is used. The minimum peak height is set to 200 calibrated ADC counts.
Afterwards, the peak positions of the channels are compared. If two or more positions match within a range of 15 ns, the integral of the pulses is calculated. For that, it is integrated over the positive part of the registered pulse in a range from 7 ns on the left to 8 ns on the right side of the detected peak positions. As explained in section 5.4, the positive part of the SiPM pulse recorded with the TARGET corresponds to the left edge of the "raw" pulse.
With the estimated size of the 1 p.e. pulse integral (see section 5.4), calculated with the same integration method, the signal sizes in p.e. can then be approximated.
The 1 p.e. pulse integral is estimated to (123 ± 9) ADC counts $\cdot$ ns at an overvoltage of 1.4 V. To translate this value to an overvoltage of 1 V, the integral is multiplied with 1 V/1.4 V. Thus, the 1 p.e. pulse integral $S_{1\mathrm{pe}}$ used here is given to:

$$S_{1\mathrm{pe}} \simeq (88 \pm 6)\,\mathrm{ADC\,counts} \cdot \mathrm{ns} \tag{5.1}$$

In the following,the coincidences found in the data are discussed at one example. Another example can be found in the appendix.
In figure 5.16, the example for a coincidence is shown. In both plots, the detection area used for the measurement series is illustrated. The black pixels are the trigger pixels. A color-coded scale is used.
In the left plot in the figure, the pulse integrals in calibrated ADC counts are shown for each pixel. If no pulse higher than 200 calibrated ADC counts was found, no integral was calculated and is therefore assumed to be zero.
In the right plot, the time difference between the signals can be seen. Thereby, 0 ns correspond to the pulse maximum detected first. If a pixel is white, no pulse higher than 200 calibrated

ADC counts was found in coincidence to the other pixels.
If a pixel is marked with two stars, the pulse is delayed in the same way as shown in figure 5.15.

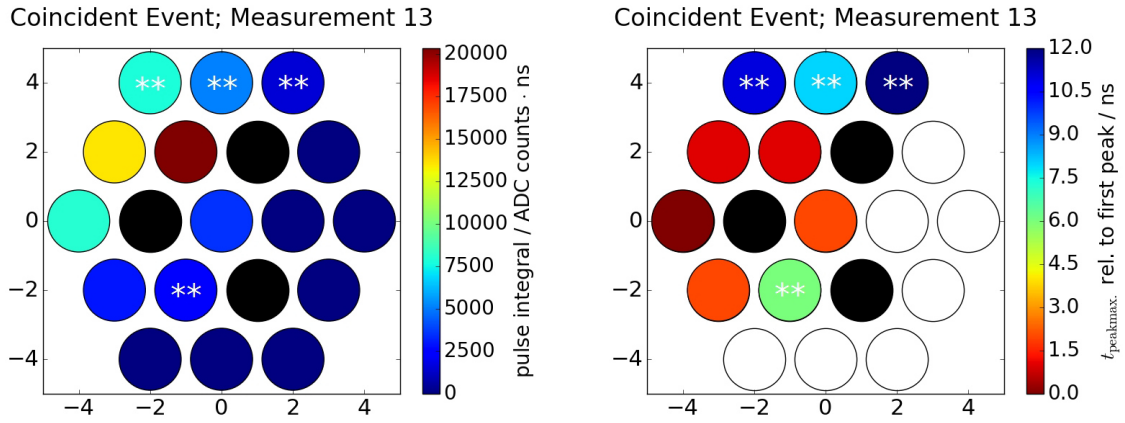

Figure 5.16.: Detected coincident event in measurement 13. **Left**: Illustration of the pulse integrals. If no pulse higher than 200 calibrated ADC counts was detected, the pulse integral for this pixel is assumed to be zero. **Right**: Illustration of the detection time (time of the detected peak maximum). The plotted time is related to the first detected peak. The black pixels are the trigger pixels. If a pixel is marked with two stars, the pulse is delayed in the same way as shown in figure 5.15.

The detected pulse integrals can be approximately translated in p.e.′s using equation 5.1:

$$\#p.e. = \frac{I}{I_{1\mathrm{pe}}}$$

For the error calculation, the error on the coincident pulses is disregarded as the fluctuation of the baseline has relatively a smaller influence on very high pulses. Therefore, the relative error on the pulse integral is again 7 %.
In figure 5.17 on the left, the translated pulse integrals are presented for the coincident event shown in figure 5.16. For a better orientation, the illustration of the detection time is shown again at the right side. It can be seen that on four pixels, at least about 90 incoming photons are registered in coincidence. On two pixels, even more than 150 incoming photons are detected with a time difference of less than 2 ns.

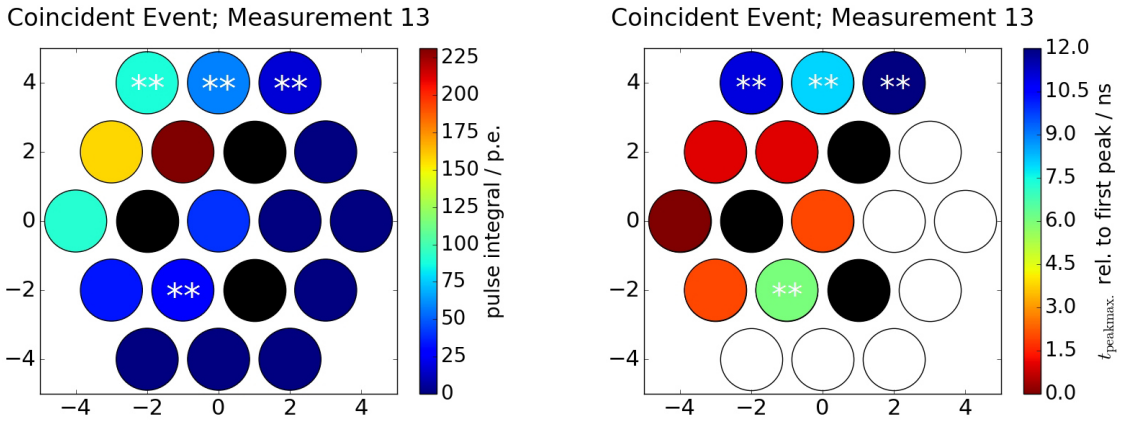

Figure 5.17.: Left: Illustration of the pulse integrals in p.e. The plot shown here corresponds to the plot in figure 5.16. If no pulse higher than 200 calibrated ADC counts was detected, the pulse integral for this pixel is assumed to be zero. **Right**: Illustration of the detection time (time of the detected peak maximum). The same illustration was already shown in figure 5.16. Discussion in the text.

As so many pixels registered such a high number of incoming photons nearly at the same time, the presented event is caused by Cherenkov light of an air shower with high probability. The probability that the night sky brightness produces such high signals of more than 100 p.e. in coincidence is very small, as the distribution of the light is random. An estimate based on simulations is given in [25].

The analysis of all measurements results in 17 coincidences on three or more pixels with a minimum pulse height of 200 calibrated ADC counts, corresponding to a pulse integral of about 1800 ADC counts · ns or approx. 20 p.e. found in the data. If all these events are counted as detected air showers, 17 air showers during a measurement time of $8 \times 5\,\text{min} = 40\,\text{min}$ are registered.

All in all, it was shown that it is possible to measure Cherenkov light of air showers with the TARGET electronics. Nevertheless, an exact calculation of the number of detected photons was not possible. Only an estimation could be done as the 1 p.e. pulse integral could only be estimated with low accuracy. The other main problem was that some pulses were cut off at the top. It should be investigated if this is really caused by a preamplifier saturation or if there are other reasons. If yes, for example a lower overvoltage of the SiPMs may reduce the rate of recorded cut- off pulses.

6. Conclusion and Outlook

The FAMOUS telescope is a prototype for a SiPM based fluorescence telescope for the detection of extensive air showers. Its camera consists of 61 pixels, each composed by a Winston cone and a SiPM. As readout electronics, the TARGET data acquisition system, originally developed for the readout of photon sensors at the Cherenkov Telescope Array (CTA), shall be used in the future.

In this bachelor thesis, 16 pixels of FAMOUS were used to implement and test the TARGET's performance.
To get an impression for the possible performance, dark rate measurements with an oscilloscope were recorded and analyzed for each pixel. Finger spectra could be created. This gave the possibility to calculate the gain and the crosstalk probability of the SiPMs.

Afterwards, the TARGET was implemented.
A possible baseline calibration method was developed and used for the following mesurements. This calibration is necessary as the baseline of TARGET fluctuates too much for precise measurements of smaller input signals.
Furthermore, Cherenkov light of extensive air showers was successfully recorded with the telescope and the TARGET. On many pixels of the camera, SiPM pulses of more than 100 p.e. were measured in coincidence. The only probable explanation for this is Cherenkov light, as it arrives in form of a light flash of a few nanoseconds length on the earth's surface.
Nevertheless, there are still problems to be solved. In contrast to the oscilloscope measurements, it was not possible to create a finger spectrum out of the data recorded with the TARGET in dark noise measurements. The reason is the high baseline fluctuation even after the calibration compared to the height of the dark noise SiPM pulses. Because of this, the pulse integral of the 1 p.e. pulse could only be roughly estimated. Additionally, the internal self trigger could and can not be used for the data recording. Therefore, the external trigger has to be used.
All in all, it was however proven that the TARGET data acquisition is suitable for the detection of extensive air showers. If the remaining problems mentioned are solved, it should be possible to analyze Cherenkov light events with higher accuracy. Also, fluorescence light should be able to detect. For that, it is however necessary to install the FAMOUS telescope outside of Aachen at a place with less background light. Otherwise, the expected detection rate is much to small to be practical.

Bibliography

[1] H. Kolanoski. Einführung in die Astroteilchenphysik: Skript der Vorlesung, 2010. `https://www-zeuthen.desy.de/~kolanosk/astro0506/skripte/cosmics01.pdf`.

[2] R. A. Mewaldt. Cosmic Rays, 1996. `http://www.srl.caltech.edu/personnel/dick/cos_encyc.html`.

[3] J. Bluemer, R. Engel, and J. R. Hörandel. Cosmic Rays from the Knee to the Highest Energies. *Prog. Part. Nucl. Phys. 63*, pages 293–338, 2009. arXiv: 0904.0725.

[4] K.A. Olive et al (Particle Data Group). *Chin. Phys. C Vol. 38*, 2014 (update 2015)(090001).

[5] K.-H. Kampert. Ultra-High Energy Cosmic Rays: Results and Prospects. 2014. arXiv: 1404.6515.

[6] P. Sommers. Ultimate Energy Particles in the Universe: Extensive Air Showers and Measurement Techniques. *C.R.Physique 5*, 2004.

[7] A. Haungs et al. KCDC – The KASCADE Cosmic-ray Data Centre. *Journal of Physics Conference Series*, 2015.

[8] F. Knuth. *Commissioning Of The Air Shower Fluorescence Telescope Prototype FAMOUS.* Bachelor Thesis, RWTH Aachen, 2014.

[9] T. Montaruli. Lecture 10: The Cherenkov Effect. `http://icecube.wisc.edu/~tmontaruli/801/lect10.pdf`.

[10] H. Alaeian. An Introduction to Cherenkov radiation, 2014. `http://large.stanford.edu/courses/2014/ph241/alaeian2/`.

[11] F. Arqueros, J. R. Hoerandel, and B. Keilhauer. Air Fluorescence Relevant for Cosmic-Ray Detection — Summary of the 5th Fluorescence Workshop, El Escorial 2007. *Nucl. Instrum. Meth. A 597*, pages 1–22, 2008. arXiv: 0807.3760.

[12] The Pierre Auger Collaboration. The Fluorescence Detector of the Pierre Auger Observatory. *Nucl. Instrum. Meth. A 620*, 2010. arXiv: 0907.4282.

[13] T. Waldenmaier, J. Blümer, and H. Klages. Spectral resolved Measurement of the Nitrogen Fluorescence Emissions in Air induced by Electrons. *Astroparticle Physics 29*, pages 205–222, 2008. arXiv: 0709.1494.

[14] J. Koschinsky. *Signal extraction from SiPM traces taken by prototype electronics developed for AugerPrime.* Bachelor Thesis, RWTH Aachen, 2015.

[15] The Pierre Auger Collaboration. The Surface Detector System of the Pierre Auger Observatory. *Nucl. Instrum. Meth. A 586*, pages 409–420, 2008. arXiv: 0712.2832.

[16] T. Bretz et al. FAMOUS- A fluorescence telescope using SiPMs. *Proceedings of Science 649*, 2015.

[17] M. Lauscher. *Characterisation Studies of Silicon Photomultipliers for the Detection of Fluorescence Light from Extensive Air Showers.* Master Thesis, RWTH Aachen, 2012.

[18] K. Höpfner. Kern- und Teilchenphysik im Bachelorpraktikum: Detektoren: Skript der Vorlesung, 2015.

[19] J. Schumacher et al. Dedicated power supply system for silicon photomultipliers. *Proceedings of Science 605*, 2015.

[20] C. Günther. *Temperature Dependence of the SiPMs and the front-end Electronics for AugerPrime.* Bachelor Thesis, RWTH Aachen, To be published 2016.

[21] Hamamatsu Corporation. What is the photon detection efficiency (PDE) of a silicon photomultiplier?, 2016. `http://www.hamamatsu.com/jp/en/community/silicon_photomultipliers/tutorials/what_is_sipm_pde/index.html`.

[22] KETEK GmbH. Device Parameters. `http://www.ketek.net/products/sipm-technology/device-parameters/`.

[23] SensL. Website of the J-Series Family. `http://sensl.com/products/j-series/`.

[24] L. Weinstock. *Development of front-end electronics for detectors with SiPM readout.* Master Thesis, RWTH Aachen.

[25] T. Niggemann. *The Silicon Photomultiplier Telescope FAMOUS for the Detection of Flouorescence Light.* Doctoral Thesis, RWTH Aachen, To be published November 2016.

[26] A. Bogner. *Trigger Implementation for FAMOUS.* Bachelor Thesis, RWTH Aachen, To be published 2016.

[27] E. Ganster. *Test des TARGET-7-Datenerfassungsmoduls für das IceACT Luft-Cherenkov-Teleskop.* Bachelor Thesis, RWTH Aachen, 2016.

[28] L. Tibaldo et al. TARGET: toward a solution for the readout electronics of the Cherenkov Telescope Array. *Proceedings of Science*, 2015. arXiv: 1508.06296v2.

[29] B. Pestka. *Commissioning of the self-Trigger of the TARGET read.out-board for FAMOUS.* Bachelor Thesis, RWTH Aachen, To be published in 2016.

[30] J. Schumacher. *Front-end Electronics for Silicon Photomultipliers.* Master Thesis, RWTH Aachen, 2014.

[31] M. Duarte. detect_peaks.py. `http://nbviewer.jupyter.org/github/demotu/BMC/blob/master/notebooks/DetectPeaks.ipynb`.

[32] A. Biland et al. Calibration and performance of the photon sensor response of FACT – The First G-APD Cherenkov telescope. *JINST 9*, (10):P10012, 2014. arXiv: 1403.5747.

Acknowledgements
Danksagungen

An dieser Stelle möchte ich mich bei allen bedanken, die mich bei der Anfertigung dieser Arbeit unterstützt haben.

Zunächst gilt mein Dank Herrn Prof. Dr. Hebbeker und Herrn Prof. Dr. Bretz, die es mir erst ermöglicht haben, diese Arbeit an ihrem Institut anzufertigen. Außerdem erklärten sie sich sofort bereit, die Erst- bzw. Zweitkorrektur zu übernehmen.

Außerdem möchte ich mich besonders bei meinem Betreuer Johannes Schumacher bedanken, der bei Fragen und Problemen immer sehr ausführlich und gut weitergeholfen hat.
Danke auch an Erik Ganster, der trotz Prüfungsvorbereitung bei Problemen mit dem TARGET gerne weitergeholfen und seine Bachelorarbeit zur Verfügung gestellt hat. Des Weiteren danke ich Christoph Günther für seine Tipps zum Auswerten der Oszilloskop-Messungen.
Auch bei meinen Bürokollegen möchte ich mich bedanken: Zunächst Benjamin Pestka, mit dem ich viele der Messungen und Auswertungen gemacht habe. Ohne ihn hätte das sicherlich nicht so gut geklappt. Außerdem Alexander Bogner, den man vor allem bei Plot-Problemen immer um Hilfe fragen konnte. Beiden danke ich auch für die gute Stimmung im Büro.
Danke auch an die Auger- und IceAct- Leute, die immer gern Fragen beantwortet haben und ein angenehmes Arbeitsklima verbreiten.

Dann möchte ich noch allen danken, die diese Arbeit oder Teile dieser Arbeit Korrektur gelesen haben: Johannes Schumacher, Kevin Janßen, Michael Weimer, Adrian Höflich und Sabrina Eilender.

Zuletzt gilt mein Dank auch meinen Freunden und meiner Familie, die mich nicht nur während der Bachelorarbeit, sondern auch im Studium immer unterstützt haben und das Studium um einiges spaßiger gemacht haben.

A. Appendix

	FACT function			
pixel no.	g, 1st meas. [V · ns]	g, 2nd meas. [V · ns]	p_{xt}, 1st meas.	p_{xt}, 2nd meas.
14	3.128±0.014	3.131 ± 0.014	0.5115±0.0056	0.5138 ± 0.0057
15	3.219 ± 0.014	3.145 ± 0.017	0.4944 ± 0.0060	0.5050 ± 0.0062
16	3.064 ± 0.018*	3.097 ± 0.015	0.4970 ± 0.0064*	0.4963 ± 0.0059
21	3.128 ± 0.014	3.129 ± 0.014	0.5214 ± 0.0061	0.5251 ± 0.0060
22	3.210 ± 0.015	3.204 ± 0.014*	0.4907 ± 0.0062	0.4875 ± 0.0060*
23	3.065 ± 0.015	3.069 ± 0.012	0.4960 ± 0.0062	0.4870 ± 0.0058
24	3.148 ± 0.014	3.133 ± 0.014	0.5030 ± 0.0059	0.5101 ± 0.0058
29	3.116 ± 0.010	3.142 ± 0.012	0.5139 ± 0.0056	0.5037 ± 0.0060
30	3.122 ± 0.013	3.148 ± 0.013	0.5261 ± 0.0060	0.5133 ± 0.0058
31	3.128 ± 0.013	3.117 ± 0.012	0.5173 ± 0.0063	0.5144 ± 0.0059
32	3.092 ± 0.017	3.077 ± 0.018	0.5052 ± 0.0064	0.5129 ± 0.0064
33	3.100 ± 0.014	3.097 ± 0.012	0.4977 ± 0.0062	0.5097 ± 0.0057
38	3.188 ± 0.013*	3.148 ± 0.013	0.4734 ± 0.0058*	0.4967 ± 0.0057
39	3.144 ± 0.012	3.165 ± 0.010	0.5007 ± 0.0061	0.4936 ± 0.0055
40	3.116 ± 0.012	3.116 ± 0.011	0.4968 ± 0.0058	0.4912 ± 0.0056
41	3.146 ± 0.014	3.153 ± 0.013	0.5109 ± 0.0062	0.5053 ± 0.0061
46	3.188 ± 0.012	3.174 ± 0.014	0.4975 ± 0.0060	0.5024 ± 0.0062
47	3.184 ± 0.012	3.157 ± 0.013	0.5127 ± 0.0058	0.5227 ± 0.0063
48	3.142 ± 0.015	3.154 ± 0.015	0.4886 ± 0.0062	0.4956 ± 0.0064
63	3.272 ± 0.013	3.273 ± 0.013	0.5070 ± 0.0062	0.5115 ± 0.0063

Table A.1.: Gain g and crosstalk probability p_{xt} of all wired pixels, calculated with the FACT function. The measurement was done with the oscilloscope. It can be seen that for most pixels, the results from both measurements fit well. Exceptions are pixel 15 and 38. For pixel 15, the gains doesn't match well, the gain of the second measurement lies in the 3.4 sigma interval of the gain of the first measurement. For pixel 38, the crosstalk probability of the second measurement only lies in the 2.9 sigma interval. As these pixels are the exceptions, they are treated as outliers. *: For a right limit on the pulse integral of 50 Vns, the optimal fit parameters couldn't be found by the fit-algorithm. The reason is, that an absolute frequency in the range from 45 to 50 was 0. As poisson errors were assumed, the error on this value is calculated to 0. Therefore, the right limit was set to 45.

Channel	# 2 p.e. pulses	# 3 p.e. pulses	#3 p.e. / # 2 p.e. [%]
0	3997	1746	44
1	3017	1328	44
2	2676	1040	39
3	3083	1100	36
4	3148	1249	40
5	3920	1678	43
6	3469	1371	40
7	3513	1380	39
8	3354	1427	43
9	3542	1613	46
10	3126	1188	38
11	3050	1257	41
12	3447	1649	48
13	3950	1688	43
14	4717	2149	46
15	5290	2402	45

Table A.2.: Corresponding to section ... Table with the number of detected assumed 2 p.e. and 3 p.e. pulses. Also, the ratio of the numbers is calculated for every channel. If the peak difference is really 1 p.e. , the ratio should be more or less equal to the crosstalk probability. The crosstalk probability is expected to be between 35 % and 50 %. The ratio lies in this range.

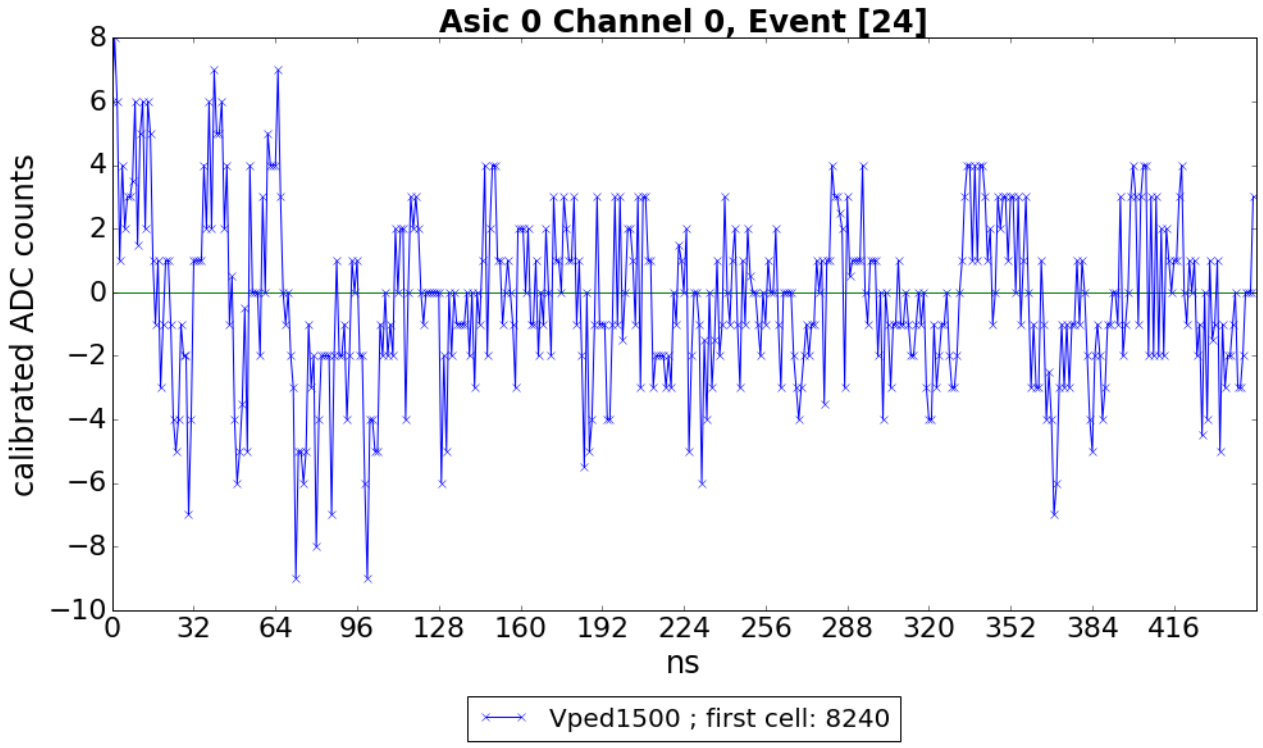

Figure A.1.: Baseline at a Vped of 1,500 corrected by the median of the baseline, considering the *structure of 32*. The fluctuation of the baseline is only a few ADC counts, but larger than for a Vped of 100.

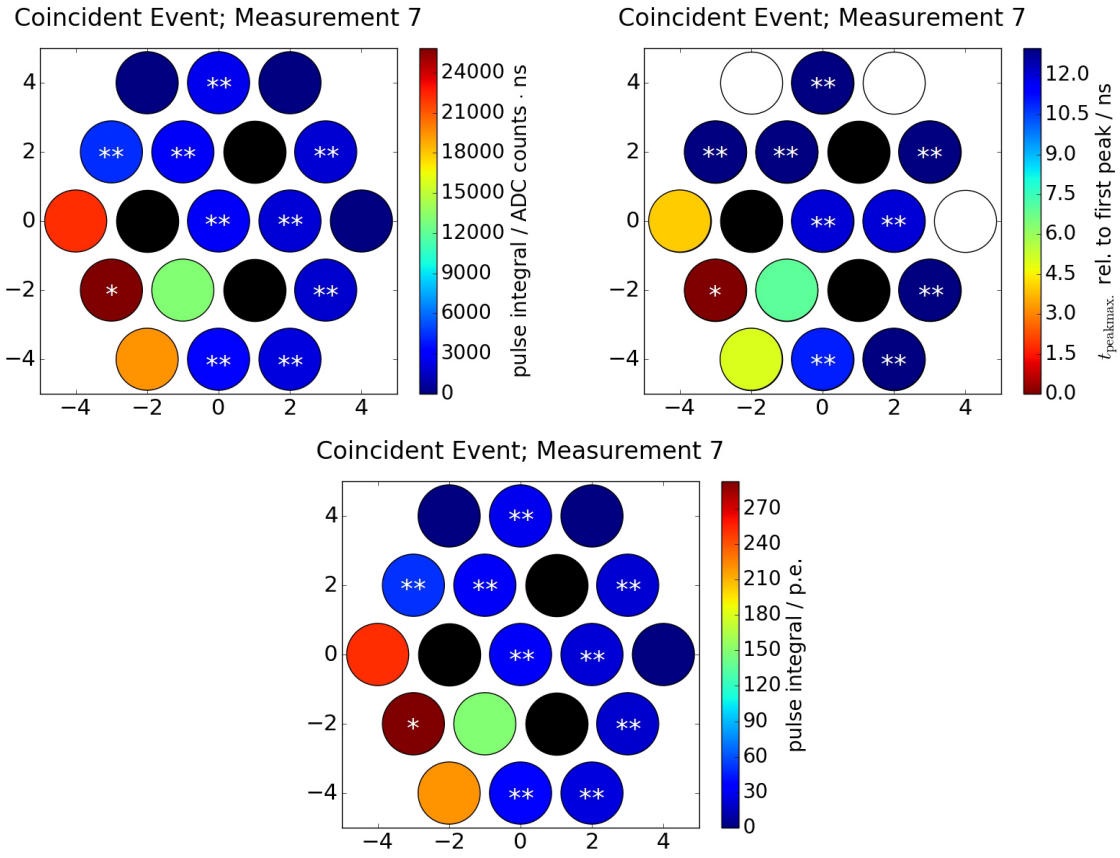

Figure A.2.: Detected coincident event in measurement 13. **Left**: Illustration of the pulse integrals. If no pulse higher than 200 calibrated ADC counts was detected, the pulse integral for this pixel is assumed to be zero. **Right**: Illustration of the detection time (time of the detected peak maximum). The given time is related to the first detected peak. **Below**: Illustration of the pulse integrals in p.e. The black pixels are the trigger pixels.
If a pixel is marked with two stars, the pulse is delayed in the same way as shown in section 5.5.2, figure 5.15 If a pixel is marked with one star, the pulse is cut off at the top. That means that the pulse height is at least the given one in the plot.

Erklärung

Hiermit versichere ich, dass ich diese Arbeit einschließlich beigefügter Zeichnungen, Darstellungen und Tabellen selbstständig angefertigt und keine anderen als die angegebenen Hilfsmittel und Quellen verwendet habe. Alle Stellen, die dem Wortlaut oder dem Sinn nach anderen Werken entnommen sind, habe ich in jedem einzelnen Fall unter genauer Angabe der Quelle deutlich als Entlehnung kenntlich gemacht.

Aachen, den 21.09.2016

Nina Laura Höflich